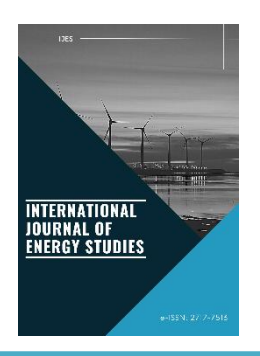
## INTERNATIONAL JOURNAL OF ENERGY STUDIES

e-ISSN: 2717-7513 (ONLINE); homepage: <a href="https://dergipark.org.tr/en/pub/ijes">https://dergipark.org.tr/en/pub/ijes</a>



Research Article

Int J Energy Studies 2025; 10(3): 743-785

Received Revised Accepted 10 Aug 2025 16 Aug 2025

DOI: 10.58559/ijes.1761941

17 Aug 2025

# CFD-based evaluation of dimethyl carbonate (DMC) combustion in CI diesel engines using experimentally validated models

#### Emrah Kantaroğlua\*

<sup>a</sup> Dept. of Mechanical Engineering, Kırıkkale University, Kırıkkale, Türkiye, ORCID: 0000-0002-6127-4318 (\*Corresponding Author: emrahkantaroglu@kku.edu.tr)

#### Highlights

- A validated 3D ICC CFD model was developed for the Renault F8Q diesel engine and used to assess the performance and emissions
  of Diesel and DMC fuels
- DMC fuel improved indicated torque and power by ~3.5% compared to Diesel, owing to better atomization, enhanced fuel—air mixing, and oxygenated combustion
- DMC reduced CO and UHC emissions significantly but caused a slight increase in NO<sub>x</sub> due to elevated in-cylinder temperatures and advanced combustion phasing

<u>You can cite this article as:</u> Kantaroğlu E. CFD-based evaluation of dimethyl carbonate (DMC) combustion in CI diesel engines using experimentally validated models. Int J Energy Studies 2025; 10(3): 743-785.

#### **ABSTRACT**

As the pursuit of sustainable energy solutions intensifies, internal combustion engines (ICEs) continue to play a vital role in heavy-duty transportation and long-distance applications. Within this framework, biofuels have gained prominence as renewable alternatives to conventional diesel, offering the potential to significantly reduce the environmental footprint of existing engine technologies. This study provides a comprehensive numerical assessment of DMC (dimethyl carbonate) in a compression-ignition (CI) engine using a thoroughly validated three-dimensional incylinder combustion computational fluid dynamics (3D ICC CFD) model. The model, developed for the Renault F8Q diesel engine, was calibrated against published experimental benchmarks and catalog specifications, ensuring high predictive reliability through extensive sensitivity analyses on mesh resolution, turbulence modeling, transient time-stepping, and heat transfer assumptions. Comparative simulations between standard diesel and the investigated DMC reveal notable shifts in combustion characteristics, performance, and emission trends. While DMC demonstrated lower unburned hydrocarbon and carbon monoxide emissions due to its inherent oxygenated composition, increases in torque and power output were observed due to increased combustion efficiency due to the oxygen in the engine, alongside a tendency for increased nitrogen oxide formation under certain operating conditions.

Keywords: CI engine, DMC, Computational fluid dynamics

#### 1. INTRODUCTION

Internal combustion engines (ICEs) remain vital to key sectors such as transportation, agriculture, and power generation worldwide [1–3]. While fossil-fuel-powered ICEs offer advantages like high energy density and operational flexibility, their extensive use significantly contributes to global greenhouse gas emissions and local air pollution [4–7]. International climate frameworks such as the Paris Agreement [7] have accelerated initiatives aimed at decarbonizing transportation. Nevertheless, projections indicate that liquid fuels will continue to meet a dominant share—approximately 85–90%—of transportation energy needs until at least 2040 [8], especially in sectors like aviation, maritime shipping, and heavy-duty transport, where energy density requirements pose major challenges to full electrification [9–12].

In response to these challenges, substantial research is underway to enhance the sustainability of existing ICEs by maintaining high power output while mitigating their environmental footprint. Within this context, dimethyl carbonate (DMC), which can be produced from various environmentally friendly sources, has emerged as a promising fuel candidate. Derived from renewable feedstocks within a carbon-neutral framework, such E-fuels have attracted increasing attention in recent years [13–20]. This article focuses on the use of dimethyl carbonate (DMC), an oxygenated compound, as an alternative to conventional diesel fuel. Pan et al. identified DMC as a promising fuel additive for enhancing combustion due to its high oxygen content (~53 wt%) and absence of carbon-carbon bonds. They also demonstrated that blending diesel fuel with 20% DMC (DMC20) results in a longer ignition delay and leads to higher peak pressure and heat release rates [21]. Yang et al. investigated the emissions behavior of diesel–DMC blends at volumetric ratios of 5%, 12.5%, 20%, and 30%. Their findings revealed that particulate matter (PM) emissions decreased by 30% to 78% as the DMC ratio increased. However, the total number of particles rose due to an increased formation of nucleation-mode particles, as the concentration of larger accumulation-mode particles diminished. While higher DMC blends (20% and 30%) caused NO<sub>x</sub> emissions to increase by 3.2% and 3.1%, respectively, no statistically significant changes were observed for lower blend levels. Carbon monoxide (CO) emissions were significantly reduced by 26.3% to 60.9%, whereas carbon dioxide (CO<sub>2</sub>) emissions and brake-specific fuel consumption (BSFC) increased with higher DMC content [22]. In another study, Kumar and Saravanan evaluated the combustion, performance, and emissions characteristics of a DMC-diesel blend containing 15% DMC (DMC15) under high load conditions, with exhaust gas recirculation (EGR) rates ranging from 0% to 30% and injection timing adjustments between 21° and 25° crank angle

before top dead center (bTDC). Their results showed that advancing injection timing to 25° bTDC improved performance but increased emissions. Conversely, at 21° BTDC and 30% EGR, the DMC15 blend achieved the longest ignition delay, the lowest peak in-cylinder pressure and heat release rate, and resulted in simultaneous reductions of 46.1% in NO<sub>x</sub> and 64.7% in smoke opacity, with only an 11.8% loss in engine performance. However, CO and total hydrocarbon (THC) emissions were found to increase under high EGR conditions [23]. Glaude et al. explored DMC's potential as a diesel oxygenate in more detail by developing a novel chemical kinetic mechanism. This mechanism was used to simulate DMC's combustion behavior in a counterflow diffusion flame and validated against existing experimental data. Their findings indicated that the decomposition rate of DMC  $\rightarrow$  H<sub>3</sub>COC(=O)O· + CH<sub>3</sub> was slower than previously anticipated due to lower-than-expected resonance stabilization in the intermediate radical. Additionally, a new molecular elimination pathway was proposed and its rate constants were calculated via quantum chemical methods. Simulations revealed that a substantial portion of DMC's oxygen content is directly converted into CO<sub>2</sub>, which limits its soot-reduction effectiveness. In an ideal oxygenate, each oxygen atom should remain bonded to a separate carbon atom to suppress soot formation, but direct CO<sub>2</sub> formation effectively wastes an oxygen atom, reducing this benefit [24]. Alzueta et al. highlighted DMC as a promising oxygenated additive due to its high oxygen content and favorable combustion characteristics. Their study involved both experimental and computational analyses of DMC oxidation behavior, soot formation tendency, and the role of NO in the reaction environment. Experiments performed under well-controlled conditions using a specially designed flow reactor showed that DMC exhibits a lower soot formation tendency compared to other oxygenates and may contribute to NO reduction under fuel-rich conditions. Modeling efforts were able to reasonably reproduce experimental results and emphasized the sensitivity of combustion predictions to the thermodynamic data of DMC and its intermediate species [25]. In their study, O'Connell et al. investigated the injection behavior of DMC and polyoxymethylene dimethyl ethers (PODE/OME). Their injection experiments revealed that, due to their lower heating values, DMC-diesel and PODE-diesel blends require either increased injection pressure or longer injection duration to achieve equivalent engine power output. Engine testing further demonstrated the potential of these additives to mitigate the particle–NO<sub>x</sub> trade-off [26].

In this context, the present study investigates the combustion and emission characteristics of DMC, one of the most promising synthetic oxygenated fuels, using an advanced three-dimensional incylinder computational fluid dynamics (3D ICC CFD) modeling framework within a compression

ignition engine platform. Simulations were performed on the well-studied Renault F8Q706 diesel engine, which operates with a direct injection system, 1870 cc displacement, and a compression ratio of 21.5:1. A fully validated CFD model was developed for this engine configuration using reported experimental data under full throttle and various engine speeds. The CFD framework includes detailed sub-models for spray dynamics, turbulence, droplet collisions, and combustion chemistry to capture the complex physical processes occurring inside the cylinder during diesel combustion. The aim of this study is to comparatively assess how each synthetic fuel affects key combustion metrics such as in-cylinder pressure, torque, indicated power (IP), indicated mean effective pressure (IMEP), indicated specific fuel consumption (ISFC), and thermal efficiency. By applying a validated CFD approach to a realistic diesel engine configuration, this research provides new insights into the potential of synthetic e-fuels like DMC to support decarbonization targets while maintaining engine performance under practical operating conditions.

## 2. THEORY AND METHODOLOGY

In this study, the combustion characteristics of diesel and DMC were investigated in a commercial compression-ignition (CI) engine using a 3D ICC CFD model. The performance and emission characteristics of the CI engine were determined using the following research methods: **Experimental data**: Obtained from literature to validate the 3D ICC CFD model. **3D ICC CFD modeling**: Conducted using ANSYS-Forte Version 25.R1 to compare the E-Fuels.

## 2.1. Engine Testing Procedure

The validation of the CFD model in this research was supported by experimental datasets previously published for the Renault F8Q diesel engine, a widely adopted powertrain in European passenger vehicles [27–30]. In the foundational work by Satgé de Caro et al. [27], the engine was tested under four fixed-speed conditions (1000, 2000, 3000, and 4000 rpm) combined with varying throttle positions ranging from 75% to full load. These operating points were chosen to encompass a representative range of real-world diesel engine duty cycles involving different speed-load combinations.

To further improve the robustness of the model, supplementary experimental results were incorporated from a study by Armas et al. [28], in which the same engine was examined using an engine dynamometer under steady-state conditions. In these tests, the engine operated across a series of constant speed and load scenarios, during which vital engine performance metrics were

measured, including brake torque, brake power, BSFC, and emission outputs such as carbon monoxide (CO), unburned hydrocarbons (UHC), nitrogen oxides (NO<sub>x</sub>), and smoke opacity. The engine's fuel system was carefully calibrated for both pure diesel and blended fuel tests, while intake air conditions were maintained under strict control. Full-load testing was employed, and incylinder pressure traces were captured as a function of crank angle. These pressure measurements were essential for evaluating combustion timing and heat release behavior—key parameters in the development of a transient 3D ICC CFD model.

Additionally, manufacturer-provided benchmark data were used to complement the validation process. According to catalog sources [29, 30], the rated engine outputs were 47 kW at 4500 rpm and 118 Nm at 2500 rpm. Figure 1 displays both assembled and disassembled views of the tested F8Q engine, a four-cylinder, 1.87-liter, turbocharged compression-ignition engine featuring a 21.5:1 compression ratio. A complete list of technical specifications used for the CFD model is presented in Table 1.











Figure 1. F8Q Engine

**Table 1.** Test engine specifications [27-31]

Specification	Description		
Engine model	Renault F8Q		
Cylinder configuration	In-line 4-cylinder		
Number of valves	8		
Type of cooling	Water cooling		
Displacement, cm <sup>3</sup>	1,870		
Compression ratio	21.5:1		
Bore x Stroke, mm	80 x 93		
Piston-to-cylinder clearance, mm	0.021-0.055		
Connecting rod length, mm	144		
Injection type	DI		
Fuel injection pump	Electric with immobilizer		
Injection nozzle pressure (Bosch), bar	135		
Valve mechanism	Single overhead camshaft		
Valve diameter (inlet), mm	36.22		
Valve diameter (exhaust), mm	31.62		
Intake valve seat angle, deg	60		
Exhaust valve seat angle, deg	45		
Intake valve opening BTDC, CAD at 2250 rpm	0		
Intake valve closing ABDC, CAD at 2250 rpm	18		
Exhaust valve opening BBDC, CAD at 2250 rpm	41		
Exhaust valve closing ATDC, CAD at 2250 rpm	0		
Max. Power, kW at 4500 rpm	47		
Max. Torque, Nm at 2250 rpm	118		

The parameters obtained from the experimental studies in the literature and compared with the 3D ICC CFD model—such as brake torque, brake power (BP), brake mean effective pressure (BMEP), BSFC, thermal efficiency, and in-cylinder pressure—are summarized in Table 3. Additionally, recorded emissions including CO, UHC, and NO<sub>x</sub> were also utilized to characterize engine behavior, as presented in Table 2.

**Table 2.** Parameters found in engine tests in literature

	Measured parameter	Calculated parameter
	Torque [29, 30]	Torque [27]
man	BP [27, 29, 30]	BMEP [29, 30]
Performan	BMEP [27, 28]	
Pe	In-Cylinder Pressure [28]	
————	CO [27]	
Emission	UHC [27]	
En	NO <sub>x</sub> [27]	

Based on these experimental results from the literature, the input parameters for the 3D ICC CFD model were defined accordingly using data obtained from these tests and references. To ensure high modeling accuracy, the complete engine geometry and boundary conditions were numerically reproduced in full consistency with both the experimental setup and catalog data.

## 2.2. Numerical Model Description for 3D In-Cylinder Combustion

In this study, the performance and emission outputs of DMC—used as e-fuel—were compared using a validated 3D ICC CFD model. The in-cylinder combustion model requires a timedependent definition represented by the crankshaft angle and includes the motion descriptions of the moving engine components. Therefore, in addition to the initial and boundary conditions, the developed model incorporates the solid model geometry of the 3D combustion chamber, motion profiles of the moving parts, reaction mechanism definitions, and mesh motion configurations. The 3D ICC CFD model developed in this study was implemented using the Ansys-Forte 25.R1 module. As shown in Table 2, engine speed, temperature, and pressure values were defined in the model based on the measurements and conditions reported in experimental studies from the literature. Furthermore, key output parameters such as torque, brake power (BP), brake mean effective pressure (BMEP), and brake-specific fuel consumption (BSFC) obtained from test results were used to validate the simulation results for the baseline diesel fuel. In addition to experimental data, sensitivity analyses were conducted to ensure appropriate selections for mesh size, time step, and sub-models for combustion, turbulence, reaction kinetics, and flame speed, thereby enhancing the accuracy of the 3D ICC CFD model. The governing operators used in the CFD model are described as follows. The mass conservation equations employed in the model are presented in Equation 1 [32-34]. In Equation 2, the momentum conservation equation is provided, which includes pressure force, viscous forces, and turbulence effects [32-34]. The conservation of energy

equations is given in Equation 3 [32-34]. The RANS RNG  $\varepsilon$ -epsilon turbulence model equation is given in Equation 4 [33-35].

$$\frac{\partial \bar{\rho}_{k}}{\partial t} + \nabla \cdot (\bar{\rho}_{k} \widetilde{\mathbf{u}}) = \nabla \cdot [\bar{\rho} D \nabla \bar{\mathbf{y}}_{k}] + \nabla \cdot \Phi + \dot{\bar{\rho}}^{c}$$
(1)

$$\frac{\partial \tilde{\rho} \tilde{\mathbf{u}}}{\partial t} + \nabla \cdot (\tilde{\rho} \tilde{\mathbf{u}} \tilde{\mathbf{u}}) = -\nabla \tilde{P} + \nabla \cdot \tilde{\boldsymbol{\sigma}} - \nabla \cdot \boldsymbol{\Gamma} + \overline{\rho} \, \overline{\mathbf{g}}$$
(2)

$$\frac{\partial \bar{\rho}\tilde{\mathbf{I}}}{\partial t} + \nabla \cdot (\bar{\rho}\tilde{\mathbf{u}}\tilde{\mathbf{I}}) = -\bar{\rho}\nabla \cdot \tilde{\mathbf{u}} - \nabla \cdot \tilde{\mathbf{J}} - \nabla \cdot \mathbf{H} + \bar{\rho}\tilde{\epsilon} + \dot{\widetilde{\mathbf{Q}}}^{c}$$
(3)

$$\frac{\partial \bar{\rho} \tilde{\epsilon}}{\partial t} + \nabla . \left( \bar{\rho} \widetilde{\boldsymbol{u}} \tilde{\epsilon} \right) = - \left( \frac{2}{3} c_{\epsilon 1} - c_{\epsilon 3} \right) \bar{\rho} \tilde{\epsilon} \nabla . \widetilde{\boldsymbol{u}} + \nabla . \left[ \frac{(v + v_T)}{Pr_{\epsilon}} \nabla \tilde{\epsilon} \right] - \frac{\tilde{\epsilon}}{\tilde{k}} \left[ c_{\epsilon 1} (\boldsymbol{\sigma} - \boldsymbol{\Gamma}) : \nabla \widetilde{\boldsymbol{u}} - c_{\epsilon 2} \bar{\rho} \tilde{\epsilon} \right] - \bar{\rho} (4)$$

In this study, 3D ICC CFD model of the F8Q engine was developed based on experimental test data available in literature. Following model validation and subsequent verification using performance parameters from the same test data, comparative fuel analyses were conducted. For this purpose, CFD model definitions were carried out in a structured sequence, and the simulations were completed accordingly. The creation of the CFD model file and the simulation workflow were conducted following the procedural steps illustrated in Figure 2.

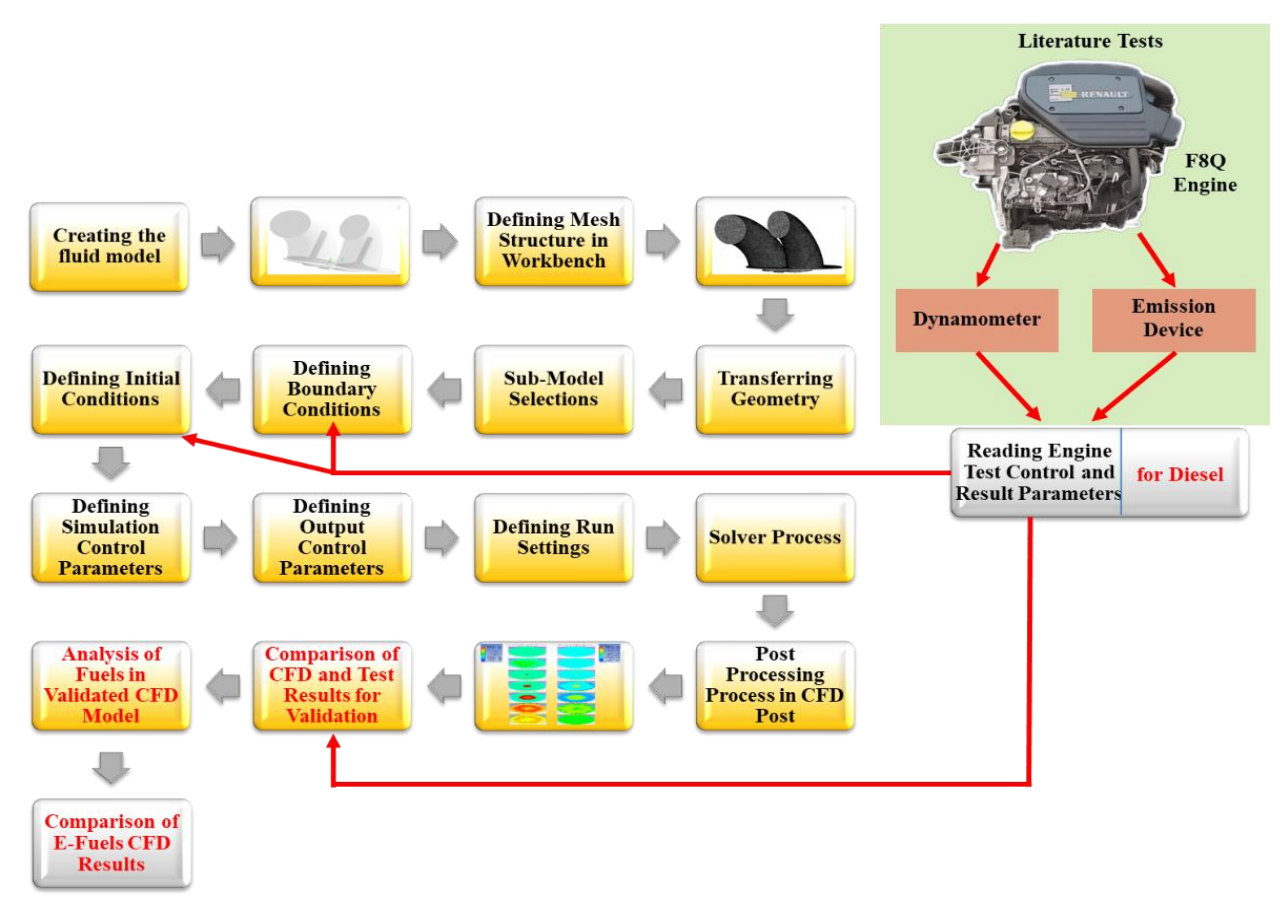
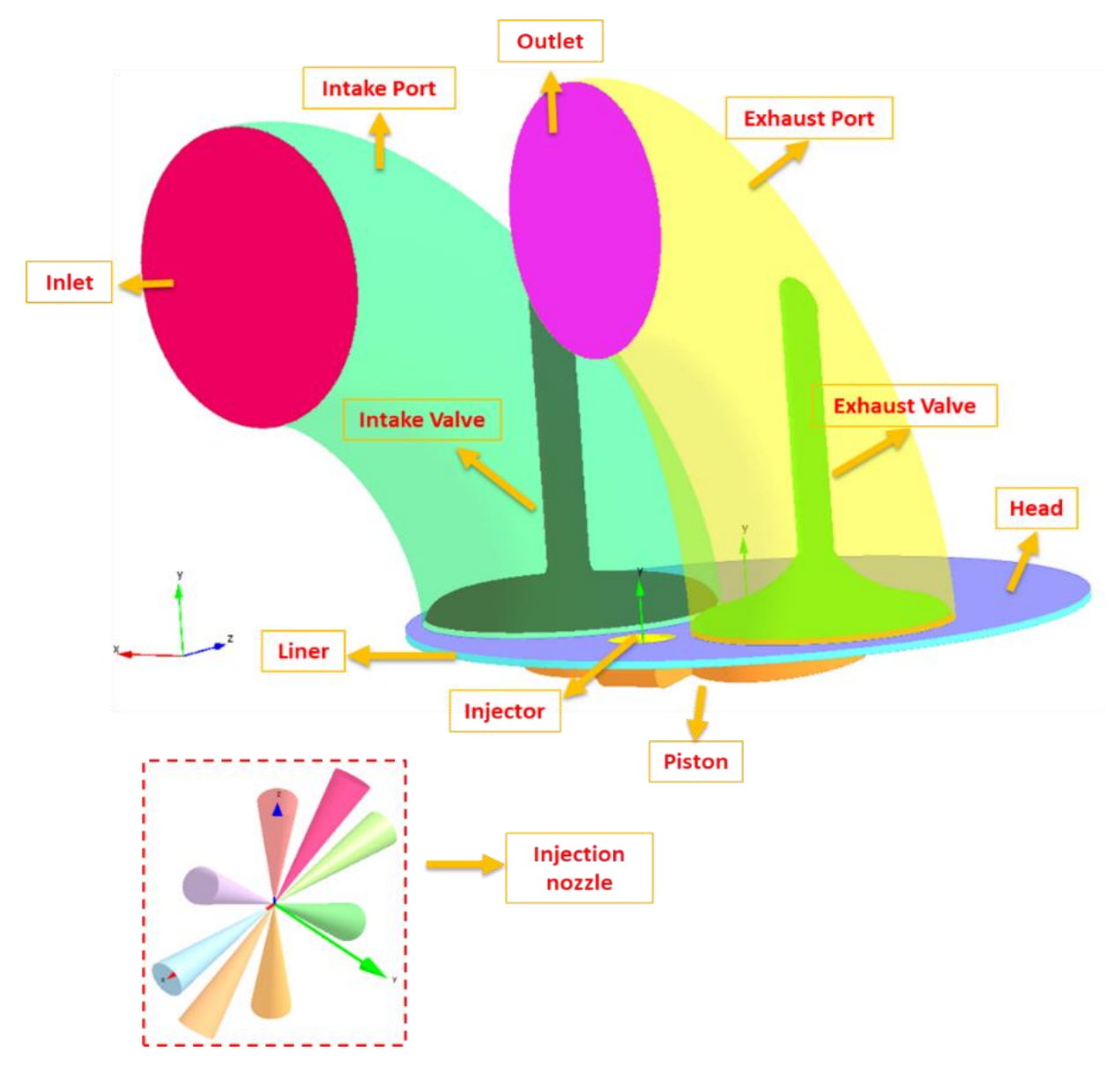


Figure 2. Steps to create 3D ICC CFD model with engine test in literature

As shown in Figure 2, the first step in the development of the 3D In-Cylinder Combustion (3D ICC) CFD model involves the creation of a solid model representing the engine cylinder's fluid domain. For this purpose, dimensional measurements were taken from the disassembled F8Q engine (illustrated in Figure 1), and the engine specifications provided in the literature [27-31] were utilized to construct the geometry using SolidWorks 2023. The model includes detailed representations of all components within a single cylinder, extending from the intake port entrance to the exhaust port exit. The geometry was created with consideration of the cyclic intervals of the CFD analysis, and the initial configuration was defined at the top dead center (TDC) position, just before the start of the intake stroke. Based on this initial piston position, the boundary surface definitions for the CFD domain were established within Ansys-Forte, as shown in Figure 3.



**Figure 3.** Boundary surfaces of in-cylinder geometry for 3D ICC CFD model of F8Q engine [34]

An essential phase in the construction of the 3D ICC CFD model for the F8Q engine involved creating the computational mesh. This process was executed within the Ansys-Workbench environment, where meticulous attention was given to generating a high-fidelity mesh that could deliver accurate and numerically stable simulation results. The detailed mesh characteristics and parameters applied during this stage are summarized in Table 3. Mesh development was informed by mesh quality assessments and independence evaluations, which helped define optimal element sizing and refinement levels. The final mesh layout, tailored for the in-cylinder combustion domain, is illustrated in Figure 4. This configuration reflects the combined outcome of the mesh setup described in Table 3 and the conclusions drawn from the mesh sensitivity analysis.

**Table 3.** Mesh metrics for 3D ICC CFD model.

Dynamic Mesh Metrics	Values
Element size, mm	0.75
Number of mesh	445,124.00-1,723,896.00
Grid topologies	Hexahedral and Polyhedral
Aspect ratio	1-2
Skewness	0.2-0.36
Quality	Orthogonal quality

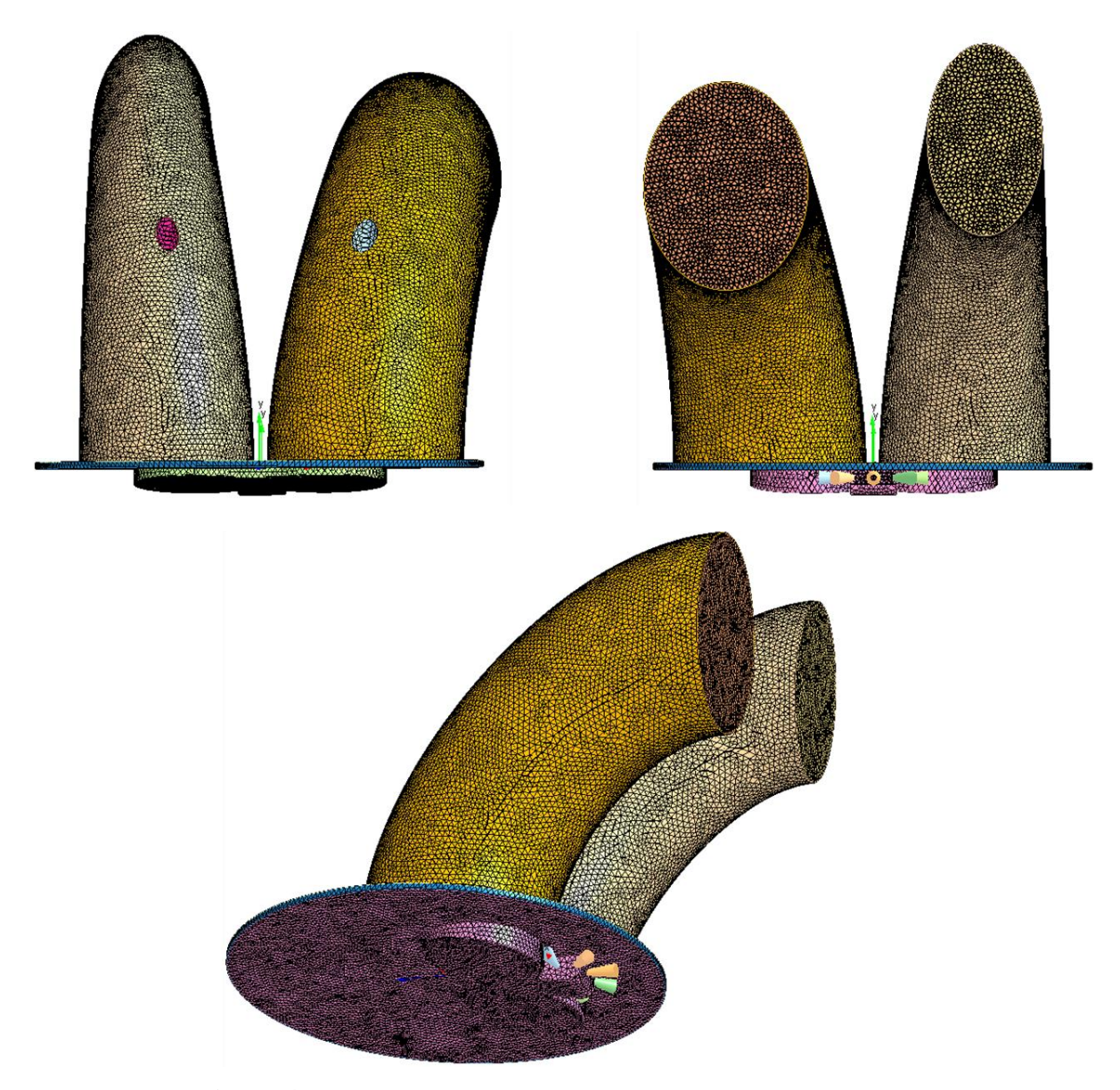


Figure 4. Mesh structure for 3D ICC CFD model of in-cylinder

The selection of physical and chemical models used in the 3D ICC CFD simulations was based on the engine configuration and combustion characteristics of direct injection charge diesel operation. Appropriate models for combustion, turbulence, flame propagation, and source terms were implemented to capture in-cylinder processes accurately. A summary of all model selections employed in the CFD framework is presented in Table 4.

Table 4. Using necessary models for 3D ICC CFD model

Models	Selected models
Combustion Regimes	Non-Premixed Turbulent Diffusion Combustion
Turbulence Model	RANS RNG k-ε
Turbulence Kinetics Interaction Model	On
Heat Transfer Model	Han-Reitz
Droplet Collision Model	Adaptive Collision Mesh Model
Injection Type	Pulsed Injection
Injection Velocity Profile	Sine Profile
Droplet Breakup Model	Taylor (KH-RT)
Active Chemistry	After Fuel Injection Starts
Unburned Calculation Method	Volume Search with Fixed Radius
Fuel Library in Chemkin-Pro	Diesel_2comp_191spsoot-pseudo-gas.cks
Source Model	Species, Momentum, Energy Sources

The definition of real-time engine operating conditions in the 3D In-Cylinder Combustion (3D ICC) CFD model is one of the most critical parameters for ensuring that the numerical predictions accurately reflect actual engine behavior. These conditions are presented in Table 5 in accordance with the boundary assignments shown in Figure 3. In particular, the intake and exhaust pressures and temperatures listed in Table 5 were obtained from previously published experimental studies conducted on this engine [27, 28, 34]. As shown in Table 5, certain parameters that are either not directly measured in tests—such as cylinder liner, piston, and injector temperatures resulting from diesel fuel combustion—or not provided within the experimental test procedures were collected from other literature sources and manufacturer catalogs [34, 36].

**Table 5.** Boundary conditions for 3D ICC CFD

Boundary	Momentum Boundary	Thermal boundary	<b>Pressure Boundary</b>
conditions	Condition	condition, K	Condition, Pa
Inlet	Wall	313 [27, 28, 37]	280,000.00 [28]
Intake Port	Wall	323 [34, 36]	-
Intake Valve	Wall with mesh movement	343 [34, 36]	-
Outlet	Wall	900 [28, 37]	100,000.00 [28]
Exhaust Port	Wall	490 [34, 36]	-
Exhaust Valve	Wall with mesh movement	500 [34, 36]	-
Head	Wall	635 [34, 36]	-
Liner	Wall	616 [34, 36]	-
Piston	Wall with mesh movement	500 [34, 36]	-
Injector	Wall	600 [34, 36]	-

In addition, the properties of the reference fuel, diesel, were directly adopted from the test studies previously conducted on the same engine as reported in the literature [28]. The properties of all fuels defined in the 3D ICC CFD model are summarized in Table 6.

Table 6. Properties of fuels

Fuel Type	Diesel	DMC
Molecular formula	$C_{12}$ - $C_{25}$	(CH <sub>3</sub> O) <sub>2</sub> CO
Cetane Number	48-57	35.5
Oxygen Content (wt. %)	0	53.3
Density (g.ml <sup>-1</sup> ) @15°C	0.82	1.06
LHV, MJ/kg <sup>-1</sup>	43.36	13.5
Boiling point (°C)	221	90
Self-ignition temperature (°C)	254	195
Latent Heat of Vaporization (kJ.kg <sup>-1</sup> )	250-290	369
Kinematic viscosity at 40 °C (mm².s <sup>-1</sup> )	3.52	5.6

Furthermore, in the development of the 3D ICC CFD model, the temperature and pressure values of the intake and exhaust gases entering and leaving the CI engine cylinder ports were also defined as initial conditions. In addition to these, the gas compositions of the intake air, injected fuels, and exhaust gases were specified as the initial mass fraction values for the gas species present in the

system. The chemical compositions of the intake air entering through the intake port, the fuels injected through the injectors, and the exhaust gases are provided in Table 7.

Table 7. Mass fractions of gases for initial conditions for 3D ICC CFD

Mass ratios o	of component gases	Diesel	DMC
SIS	$C_{12}H_{26}$	0.06280	-
Fuels	(CH <sub>3</sub> O) <sub>2</sub> CO	-	0.17935
Air	$O_2$	0.21828	0.19114
Inlet Air	$N_2$	0.71891	0.62951
Gas	CO <sub>2</sub>	0.19473	0.26288
aust	H <sub>2</sub> O	0.08636	0.10761
Exhaust	$N_2$	0.71891	0.62951

As a result of the model development, the injector configuration was defined on the cylinder head in accordance with the direct injection operating principle, as illustrated in Figure 3. In this configuration, a spray system consisting of eight nozzles was implemented, with each nozzle generating conical fuel sprays. The droplet collision behavior was modeled using the Adaptive Collision Mesh Model, as previously indicated in Table 4. The ignition process was simulated with the Pulsed Injection ignition type. The inflow droplet temperature was set at 310 K, while the injector surface temperature was specified as 600 K, as presented in Table 5. For the spray dynamics, a cone angle of 15 degrees was assigned, and the droplet size distribution was defined using a shape parameter of 2.3 with an initial Sauter Mean Diameter of 40 µm. The piston motion followed a full engine cycle of 720 crank angle degrees (CAD), with the expansion stroke commencing accordingly. The fuel injection event was initiated at 697.5 CAD, with an injection duration of 7.75 degrees. A sine profile was applied for the injection velocity profile to represent the injection dynamics. The fuel injection quantities for each case were provided previously in Table 7. This injector and spray configuration allowed for accurate modeling of the fuel-air mixing and subsequent combustion processes under the direct injection combustion regime used in the 3D ICC CFD simulations.

Table 8 presents the simulation control and solution setup parameters for the 3D ICC CFD model of the CI engine. The simulation was performed to capture the entire four-stroke engine cycle, covering a total simulation range from 320 to 1080 crank angle degrees (CAD), while the full cycle

range was defined between 360 and 1080 CAD. The engine speed during the simulations was set to 2250 rpm, representing the target operating condition for the validation case. The time integration was controlled using an initial simulation time step of  $5.05 \times 10^{-5}$  seconds, with the maximum allowable simulation time step limited to  $1.00 \times 10^{-5}$  seconds to ensure numerical stability and accuracy. The SIMPLE (Semi-Implicit Method for Pressure Linked Equations) algorithm was employed as the primary solution scheme throughout the calculations. This pressure-based numerical method is widely used for solving the Navier-Stokes equations governing fluid flow and heat transfer processes in CFD simulations, and it ensures stable convergence during transient engine cycle simulations.

**Table 8.** Boundary conditions for 3D ICC CFD

Simulation Control and Solution Definitions	Value
Simulation Range, CAD	320-1080
Cycle Range, CAD	360-1080
Engine Speed, rpm	2250
Initial Simulation Time Step, s	5.05E-05
Maximum Simulation Time Step, s	1.00E-05
Solution Algorithm	SIMPLE

The sensitivity analyses applied to the selected parameters and models are summarized in Table 9. The outcomes of these sensitivity evaluations, which were carried out following the procedures specified in Table 9, are discussed in the results section. For the purposes of this study, the optimal modeling configurations were determined to enable the comparative assessment of E-Fuels.

Table 9. CFD matrix

Method	Fuels	Full Load (%)	Speed (rpm)	Number of Mesh	Simulation Time Step (s)	Turbulence Model	Heat Transfer Model
Fuels	Diesel	100	2250	445,124	1.00E-05	RANS RNG k-ε	Han-Reitz Model
Fū	DMC	100	2250	445,124	1.00E-05	RANS RNG k-ε	Han-Reitz Model
т.	Diesel	100	3175	445,124	1.00E-05	RANS RNG k-ε	Han-Reitz Model
ation	Diesel	100	4500	445,124	1.00E-05	RANS RNG k-ε	Han-Reitz Model
/alid	Diesel	75	2250	445,124	1.00E-05	RANS RNG k-ε	Han-Reitz Model
Test validation	Diesel	75	3175	445,124	1.00E-05	RANS RNG k-ε	Han-Reitz Model
L	Diesel	75	4500	445,124	1.00E-05	RANS RNG k-ε	Han-Reitz Model

	Diesel	100	2250	202,329	1.00E-05	RANS RNG k-ε	Han-Reitz Model
sis	Diesel	100	2250	979,273	1.00E-05	RANS RNG k-ε	Han-Reitz Model
Analysis	Diesel	100	2250	2,154,401	1.00E-05	RANS RNG k-ε	Han-Reitz Model
	Diesel	100	2250	445,124	2.50E-06	RANS RNG k-ε	Han-Reitz Model
itivil	Diesel	100	2250	445,124	5.00E-06	RANS RNG k-ε	Han-Reitz Model
Sensitivity	Diesel	100	2250	445,124	2.00E-05	RANS RNG k-ε	Han-Reitz Model
Model	Diesel	100	2250	445,124	1.00E-05	RANS standard k-	Han-Reitz Model
$\Sigma$	2.2.2			- ,		3	
	Diesel	100	2250	445,124	1.00E-05	RANS RNG k-ε	Amsden Model

#### 3. FINDINGS and DISCUSSION

In this study, the effects of utilizing diesel and DMC fuels in the Renault F8Q diesel engine were investigated using a fully validated 3D ICC CFD model. The model was developed and validated based on experimental test data previously reported in the literature for the same engine. Throughout both the experimental comparison and the CFD model validation processes, diesel fuel was used as the reference fuel. Following the completion of the model validation, the fuel comparison simulations were performed under engine operating conditions of 2250 rpm and full load.

In this study, comprehensive sensitivity analyses were performed to determine the optimal configuration of the 3D ICC CFD model developed for the Renault F8Q engine. Since different modeling strategies and parameter selections can considerably affect the accuracy of in-cylinder combustion simulations, a series of sensitivity studies were systematically conducted throughout the model development phase, following the evaluation of engine test data. During these analyses, key model parameters and numerical settings were varied to observe their influence on the simulation results. The obtained outputs were then compared with both catalog data and previously published experimental measurements for the same engine, enabling a robust validation of the numerical model. Following these assessments, the most appropriate model definitions were finalized to achieve the highest consistency with the reference data. The conducted sensitivity studies addressed several critical modeling components, including variations in mesh density (evaluated across four grid resolutions), time step sizes (four different increments), turbulence models (two options), heat transfer models (three options), as summarized in Table 9. In total, five test validations, eight model sensitivity analysis and two fuel comparison simulations were conducted, following the analysis matrix defined in Table 9.

### 3.1. Mesh Independency

To ensure that the CFD predictions are independent of mesh resolution, a mesh sensitivity analysis was conducted for the F8Q direct injection diesel engine. The simulations were carried out starting from 320 CAD using four progressively refined mesh densities: 202,329; 445,124; 979,273; and 2,154,401 cells. Each mesh level was generated by refining the previous mesh, thereby allowing a systematic investigation of the grid resolution effect on combustion and thermal performance. Figure 5 presents both the in-cylinder temperature distributions after combustion and the corresponding variations in thermal efficiency for each mesh configuration. The temperature contours were extracted at 720 CAD, corresponding to top dead center (TDC), and displayed in a radial cross-section to capture spatial temperature gradients at the critical piston position. As the mesh was refined, noticeable improvements in thermal efficiency were observed. Specifically, thermal efficiency increased from 0.440 for the coarsest mesh (202,329 cells) to 0.519, 0.523, and 0.525 for the subsequent mesh levels, respectively. While the improvement between the two coarsest meshes was substantial, the efficiency differences between the two finest grids were less than 1%, suggesting numerical convergence had been achieved at finer mesh densities. In addition to thermal efficiency, the chemical heat release rate (CHRR) profiles were analyzed to further evaluate the mesh resolution effect on combustion accuracy. CHRR, which characterizes the energy release rate during combustion, provides a direct indication of combustion completeness and temporal dynamics. As illustrated in Figure 5, the CHRR curves for the finest three meshes (445,124; 979,273; and 2,154,401 cells) show excellent agreement with nearly overlapping profiles, confirming stable and consistent combustion representation. In contrast, the coarsest mesh produces a significantly delayed and lower CHRR peak, indicating its inability to fully capture the combustion process dynamics. Taken together, the consistency observed in thermal efficiency, temperature fields, and CHRR trends demonstrates that the mesh containing approximately 445,124 cells offers a satisfactory compromise between computational cost and solution accuracy for the present 3D ICC CFD diesel engine simulations.

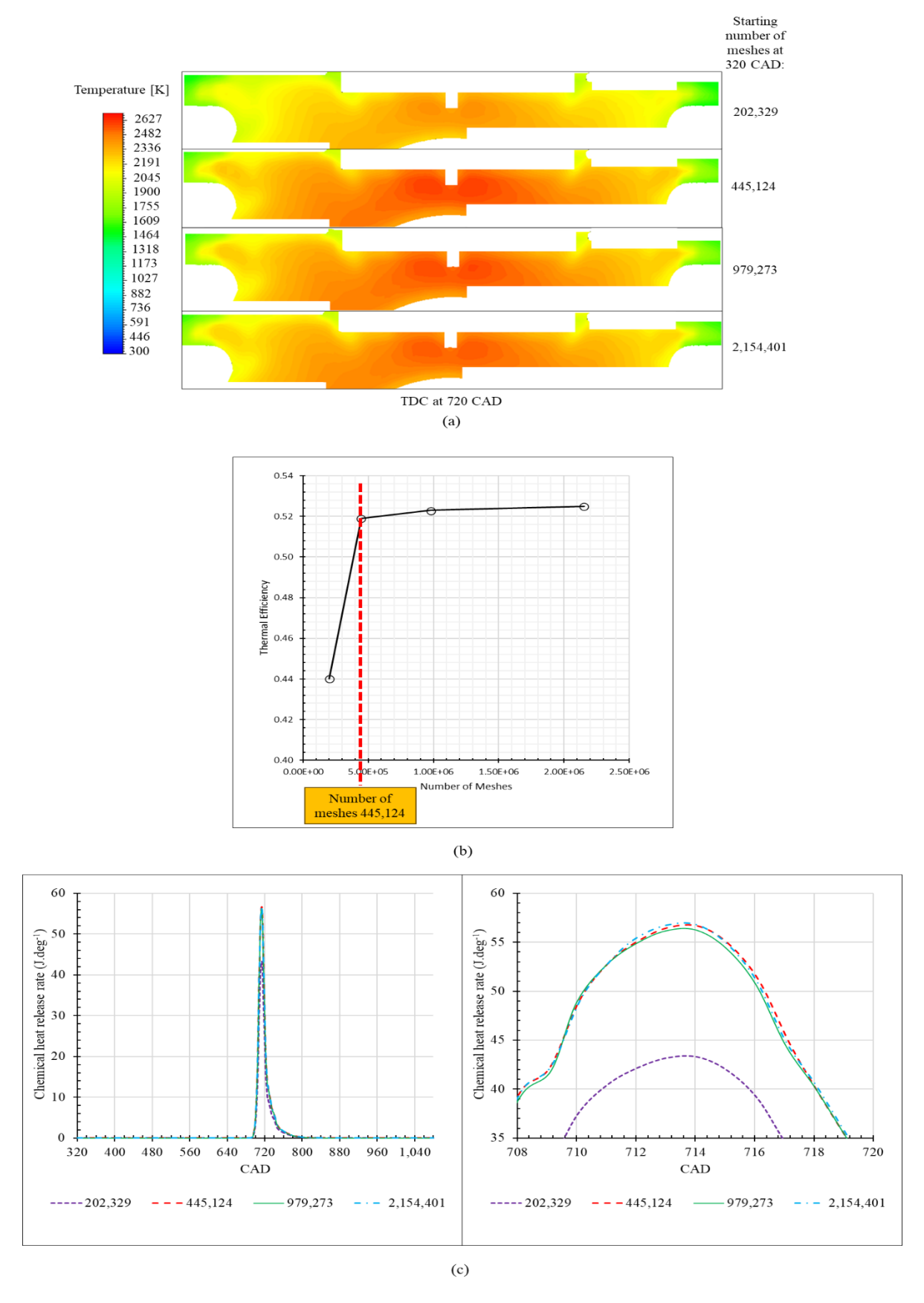


**Figure 5.** Mesh independence test for 3D ICC CFD Model (a) in-cylinder temperature axial contours, (b) thermal efficiency, (c) CHRR-CAD

### 3.2. Time Step Independency

In the transient simulations of the in-cylinder combustion process, selecting an appropriate time step size plays a crucial role in accurately resolving combustion events while maintaining computational efficiency. A smaller time step enhances the temporal resolution of rapid combustion processes, yet significantly increases the computational cost. Therefore, the time step selection must reflect the dominant physical and chemical processes occurring within the combustion chamber, particularly in relation to piston motion, valve operations, and chemical reaction kinetics. For the F8Q diesel engine operating at 2250 rpm, a complete 720 crank angle degree (CAD) cycle corresponds to approximately 0.0384 seconds. During this cycle, the piston experiences significant velocity variations, with peak piston speeds occurring near 90° crank angles after the top dead center (ATDC), corresponding to the expansion stroke's maximum velocity region. The intake valve opens at top dead center (TDC, 0 CAD) and closes at 18° after bottom dead center (ABDC), providing an intake duration of approximately 198 CAD, equivalent to ~0.0105 seconds. The exhaust valve opens at 41° before bottom dead center (BBDC) and closes at TDC, resulting in an exhaust duration of 221 CAD (~0.0117 seconds). Within these narrow periods, especially near the top dead center, rapid combustion occurs where turbulent mixing, spray evaporation, and detailed chemical reactions interact simultaneously. The combustion event itself is highly concentrated near TDC, typically within a window of 30-40 CAD, lasting approximately 0.0016 to 0.0021 seconds. During this phase, thousands of elementary reactions involving multiple chemical species occur concurrently, which demands fine temporal resolution for accurate capture of ignition delay, flame propagation, and heat release rates. To investigate the effect of time step size on numerical stability and solution accuracy, a systematic time-step sensitivity study was conducted. The CFD software dynamically adjusts the local time step based on variations in flow properties and combustion progress; however, the maximum allowable global time step remains a controlling parameter. In this analysis, simulations were performed using four distinct time step values: 2.50E-06 s, 5.00E-06 s, 1.00E-05 s, and 2.00E-05 s. The simulation results are presented in Figure 6. The thermal efficiency values corresponding to these time steps were calculated as 0.518, 0.521, 0.519, and 0.482, respectively. As shown, thermal efficiency remains relatively stable across the time steps of 2.50E-06 s to 1.00E-05 s, with only minor variations. However, a significant drop in thermal efficiency was observed at the largest time step of 2.00E-05 s, indicating under-resolved combustion behavior at coarser temporal resolution. Additionally, in-cylinder temperature distributions extracted at 720 CAD (TDC) were analyzed to assess flame structure development under different time-step configurations. As illustrated in

Figure 6, the flame front becomes poorly resolved and less intense at the highest time step, while consistent and well-defined flame structures are maintained for time steps up to 1.00E-05 s. Further insight into combustion dynamics was obtained by evaluating the chemical heat release rate (CHRR) profiles. The CHRR results revealed that for time steps ranging from 2.50E-06 s to 1.00E-05 s, the heat release profiles exhibit strong agreement with nearly overlapping peaks occurring near 714 CAD. These profiles indicate consistent combustion phasing and complete combustion at these finer time steps. Conversely, the 2.00E-05 s time step resulted in a delayed, broadened, and significantly flattened CHRR profile, suggesting incomplete combustion and degraded temporal resolution of the reaction progress. Considering all evaluation metrics—including thermal efficiency, temperature contours, and heat release profiles—a time step of 1.00E-05 s was selected as the optimal value for subsequent simulations. This choice offers a well-balanced trade-off between numerical accuracy and computational cost, while preserving the physical fidelity required to capture the complex transient combustion phenomena in the F8Q diesel engine.

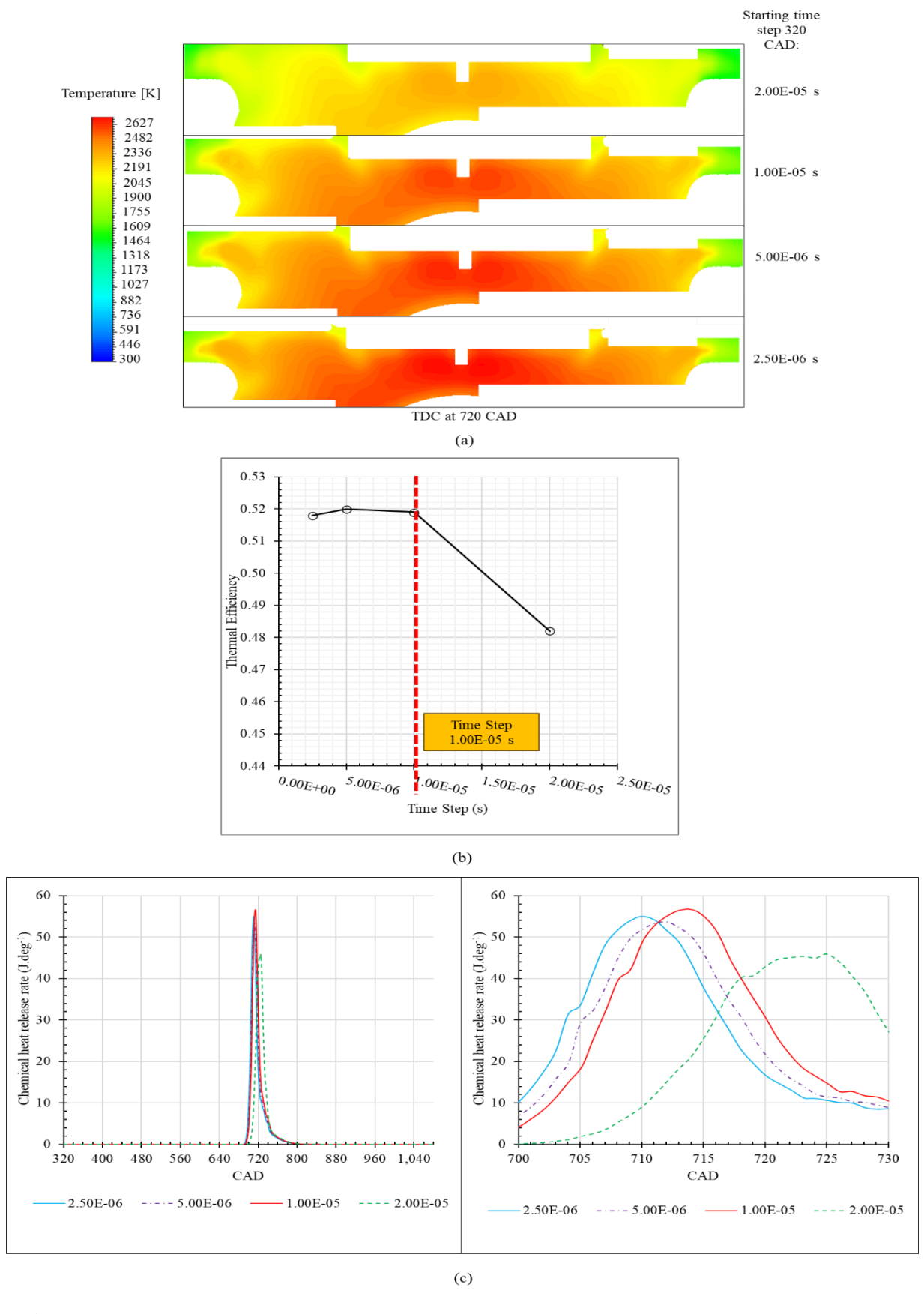


**Figure 6.** Time speed independence test for 3D ICC CFD Model (a) in-cylinder temperature axial contours, (b) thermal efficiency, (c) CHRR-CAD

## 3.3. Turbulence Model Sensitivity

In this study's CFD simulations, the turbulence behavior within the combustion chamber was primarily captured using the RANS-based RNG k-E model, due to its widespread validation and successful application in diesel engine research [38–42]. The Reynolds-Averaged Navier–Stokes (RANS) methodology separates flow variables into time-averaged and fluctuating components, enabling the resolution of turbulent characteristics with relatively low computational demand. Both the standard k-ε and RNG k-ε models extend the ε-equation by incorporating additional correction terms that address the effects of compressibility, flow expansion, and varying strain rates—key aspects in high-pressure, spray-driven combustion processes [43]. Given that the Renault F8Q engine utilizes a direct injection system characterized by intense turbulence from spray dynamics, the adoption of large eddy simulation (LES) techniques was avoided. As previously noted in the literature [44], LES methods demand extremely fine mesh resolutions to accurately resolve small-scale eddies and their flame interaction, making them less practical under current meshing constraints. Therefore, RANS models were deemed more suitable for achieving a balance between fidelity and computational efficiency in this work. To evaluate how the turbulence model selection impacts combustion prediction, simulations were performed using both the standard and RNG versions of the k-\varepsilon model. Results, depicted in Figure 7, indicate that the RNG k-\varepsilon model yielded higher thermal efficiency (0.519) compared to the standard model (0.494). This improvement is likely due to the RNG formulation's superior capacity to capture fine-scale turbulence effects that influence spray breakup and fuel-air mixing. Additionally, temperature distributions at 720 CAD revealed that the RNG k-E model predicts more intense and focused hightemperature regions, particularly at the combustion core, suggesting more efficient heat release. The chemical heat release rate (CHRR) analysis also supported this finding, as the RNG k-ε model showed an earlier and more pronounced peak, indicating faster and more complete combustion. In contrast, the standard model's broader and delayed CHRR profile suggested weaker turbulencechemistry interactions. Taking into account all combustion and performance indicators, the RNG k-ε turbulence model proved to be the more accurate and robust choice for simulating the F8Q diesel engine in this investigation, confirming similar trends reported in prior studies [42, 44].

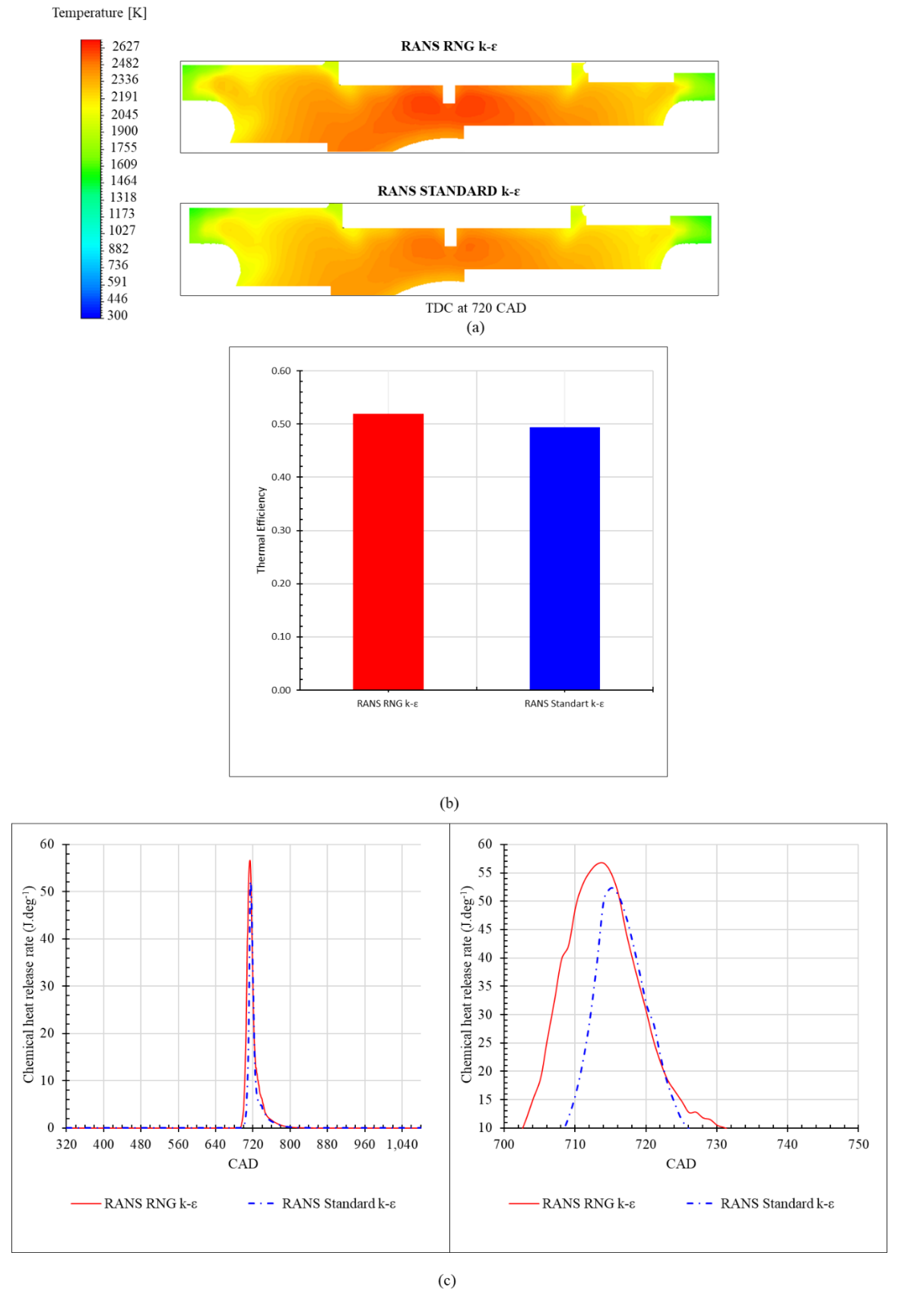


**Figure 7.** Turbulence model sensitivity for 3D ICC CFD Model (a) in-cylinder temperature axial contours, (b) thermal efficiency, (c) CHRR-CAD

## 3.4. Heat Transfer Model Sensitivity

In addition to turbulence, spray, and chemical reaction modeling, accurately representing wall heat transfer is essential for predicting combustion characteristics in diesel engines. Heat transfer directly influences flame propagation, in-cylinder temperature distribution, and overall thermal efficiency, especially in spray-dominated direct injection engines such as the Renault F8Q. In this context, two widely used heat transfer models—Han-Reitz and Amsden—were comparatively evaluated to assess their suitability for the developed 3D ICC CFD model. The Han-Reitz model is specifically designed for high-pressure, spray-driven combustion environments and accounts for both piston-induced turbulence and spray-generated mixing, which play a dominant role in diesel engines [38]. In contrast, the Amsden model, adapted from the classical Woschni formulation, primarily relies on empirical relationships involving cylinder pressure, gas temperature, and piston speed, while neglecting direct spray-turbulence interactions [45]. The results of the heat transfer model sensitivity analysis are presented in Figure 8. As illustrated, noticeable differences emerge between the two models in terms of both global thermal performance and local combustion behavior. The thermal efficiency obtained with the Han-Reitz model was calculated as 0.519, while the Amsden model yielded a lower value of 0.475. This reduction in efficiency for the Amsden model can be attributed to its limited capacity to resolve spray-induced turbulence effects and localized heat transfer gradients, which are critical under diesel combustion conditions. Further insights into the models' behavior were gained by examining the in-cylinder temperature distributions at top dead center (TDC, 720 CAD), shown in Figure 8a. The Han-Reitz model predicted significantly higher localized temperature regions within the combustion chamber, particularly near the piston bowl, where fuel spray impingement and turbulent mixing intensify heat transfer. In contrast, the Amsden model resulted in a more diffused temperature field with lower peak temperatures, reflecting its less detailed representation of spray-induced convective heat transfer. The impact of heat transfer modeling on combustion phasing was also evaluated by analyzing the chemical heat release rate (CHRR) profiles (Figures 8b and 8c). The Han-Reitz model produced a sharper and earlier CHRR peak, closely aligned with the rapid ignition and combustion expected in spray-dominated diesel operation. This reflects the model's ability to capture localized flame front development and faster heat release. Conversely, the Amsden model generated a delayed and broader CHRR profile with reduced peak intensity, indicating slower combustion and incomplete resolution of the rapid heat release phase. The superior predictive capability of the Han-Reitz model in this study can be attributed to its enhanced treatment of sprayturbulence interaction, droplet-wall impingement, and swirl-induced boundary layer thinning, all

of which are highly influential in the F8Q diesel engine configuration. This behavior is consistent with previous findings that emphasize the importance of incorporating spray-driven turbulence into heat transfer modeling for accurate diesel combustion simulations [38]. Based on these evaluations, the Han-Reitz model was selected for all subsequent simulations due to its superior ability to represent the complex heat transfer mechanisms inherent in spray-driven diesel combustion.

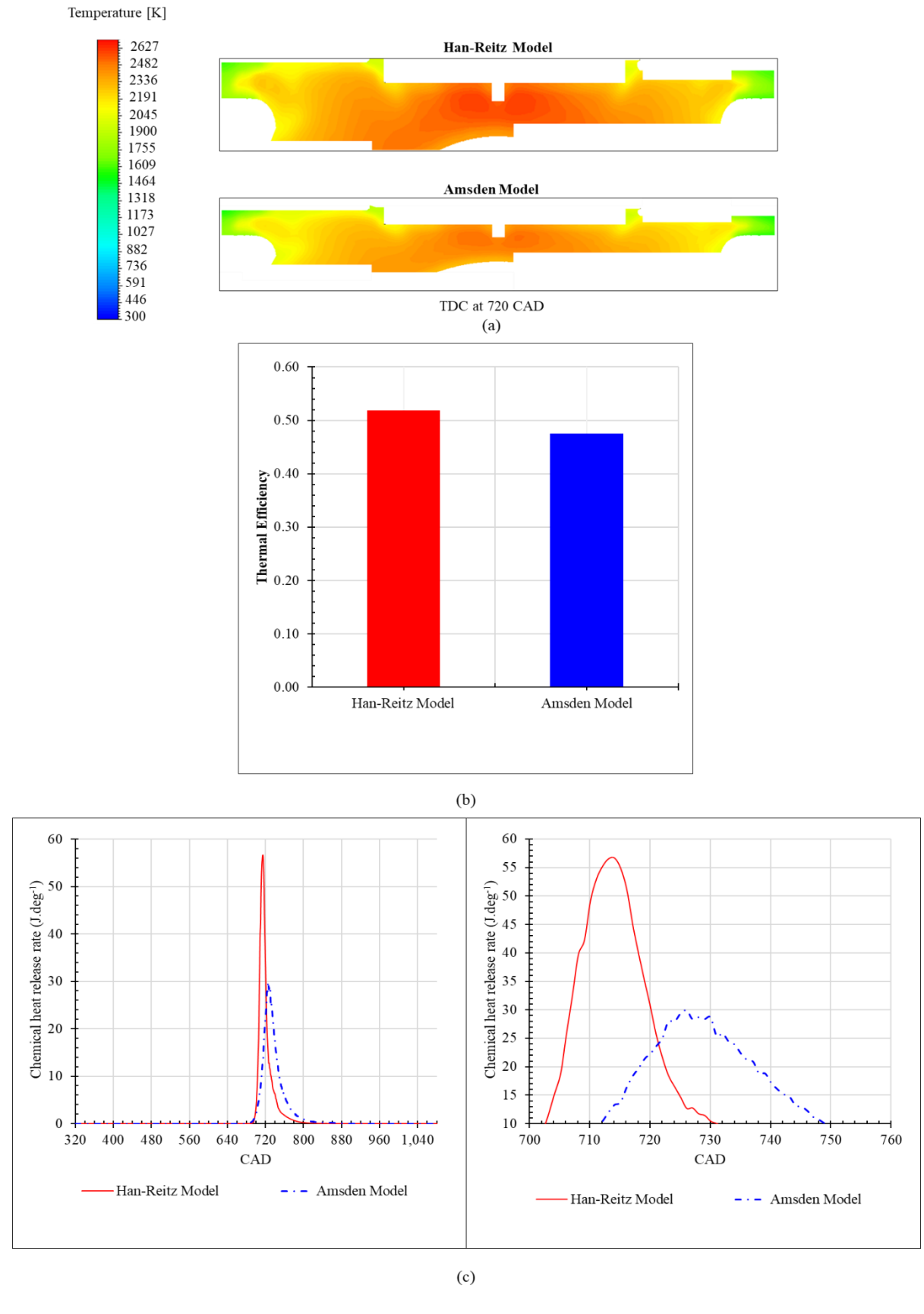


**Figure 8.** Heat transfer model sensitivity for 3D ICC CFD Model (a) in-cylinder temperature axial contours, (b) thermal efficiency, (c) CHRR-CAD

## 3.5. 3D ICC CFD Model and Test Comparison

In this study, in addition to the model sensitivity analyses, the boundary and initial conditions of the 3D ICC CFD simulations were defined based on previously published engine test data in the literature [27,28]. The parameters available from these engine tests were earlier summarized in Table 2. As can be seen, critical engine characteristics such as effective torque, BP, BMEP, incylinder pressure, and emissions including NO<sub>x</sub>, CO, and UHC were used to perform validation studies, as detailed in Table 9. In accordance with these literature test datasets, combustion simulations were conducted for the same 3D ICC CFD model under 75% and 100% throttle conditions at engine speeds of 2250, 3175, and 4500 rpm. The outcomes of these simulations represent indicated engine performance parameters. However, the experimental data reported in the literature provides brake engine characteristics. Therefore, to ensure a meaningful comparison between the CFD model results and the literature test data, it was necessary to convert the simulated indicated performance data to brake equivalents by determining the engine's mechanical efficiency. For this purpose, the mechanical efficiency of the F8Q engine was calculated using the Willans Line method, based on the BMEP-fuel consumption graph previously published by Satgé de Caro et al. [27]. As illustrated in Figure 10, this approach enabled the estimation of frictional losses without requiring additional engine tests by considering the resistive forces resulting from the inertia of the moving engine components [46]. A linear regression was applied to the BMEPfuel consumption curve, yielding a frictional BMEP value of 1.621 bar. Given that the engine was operated at 3175 rpm and produced a BMEP of 7.049 bar, the mechanical efficiency was calculated to be 0.813 based on the regression method illustrated in Figure 9. Accordingly, the engine performance parameters obtained from the 3D ICC CFD model were translated from indicated values to brake values, allowing for accurate comparison with the test data reported in the literature.

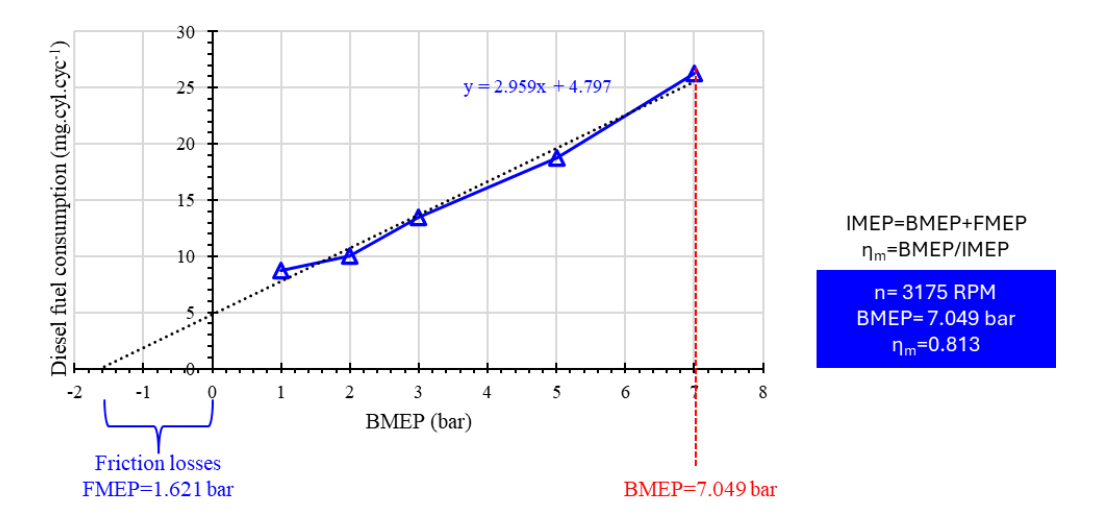


Figure 9. Williams Line method for calculating mechanical efficiency

Prior to investigating the effects of DMC utilization in the F8Q engine, the consistency of the engine's brake characteristics was verified by comparing simulation results obtained from the 3D ICC CFD model under identical operating conditions. Following an extensive series of model sensitivity analyses, the finalized 3D ICC CFD model was validated against experimental data and subsequently subjected to all necessary CFD procedures to ensure modeling accuracy. The validation of key engine performance parameters—such as brake torque, brake power, and brake thermal efficiency—is presented in Figure 10, confirming the model's predictive capability under real engine conditions at full load and given speeds. Additionally, Figure 11 illustrates the incylinder pressure validation, providing a further benchmark for combustion accuracy. As a complementary validation criterion, Figure 12, Figure 13, and Figure 14 presents the emission comparisons for NO<sub>x</sub>, CO, and UHC, which serve as important indicators of correct combustion phasing and completeness within the CFD framework. The consistency of the 3D ICC CFD model with experimental findings was evaluated through several key performance and combustion indicators. Figures 10 through 15 illustrate the model's alignment with literature data regarding brake power, in-cylinder pressure, and exhaust emissions (NO<sub>x</sub>, CO, UHC) under multiple operating conditions. Figure 10 demonstrates the correlation between the CFD-predicted brake power and reference values from both engine catalog data and previous studies [27,28]. The CFD predictions slightly overestimate the brake power, particularly at higher engine speeds (e.g., 4500 rpm), but overall follow the same trend observed in the literature. These differences can be primarily attributed to the assumptions made in the numerical model regarding combustion efficiency, heat losses, and friction, which may be idealized compared to the real engine operation. Figure 11 compares the in-cylinder pressure profiles obtained from the CFD model with experimental data reported by Armas et al. [28]. While the general pressure rise and peak pressure location near top dead center (TDC) are accurately predicted, minor discrepancies appear in the pressure decay phase. These variations can result from idealized combustion chamber wall conditions and simplifications in the heat transfer model used in the simulation.

Figure 12 shows the validation results for  $NO_x$  emissions. Although the predicted trend aligns well with literature data at 75% throttle opening [27], the CFD model tends to slightly overpredict  $NO_x$  levels at higher engine speeds. This is likely due to the model's sensitivity to in-cylinder temperature distribution and residence time, which directly influence thermal NO formation pathways. The assumption of a homogenous charge and idealized post-combustion mixing in the simulation can exaggerate the local high-temperature zones.

Figure 13 presents the comparison for CO emissions at 75% throttle opening on condition. The CFD-predicted values are consistently higher than those obtained experimentally. This overestimation may stem from limitations in modeling the late-cycle oxidation of CO, especially under rich combustion conditions or during quenching near the walls. Furthermore, simplifications regarding fuel spray-wall interactions and flame quenching mechanisms may contribute to the CO prediction deviation.

Figure 14 evaluates UHC emissions at 75% throttle opening on condition. Similar to CO, the UHC levels predicted by the CFD model are above the values reported in the experiments. This can be explained by the challenges in resolving crevice volumes and wall film behaviors in the 3D simulation, which play a significant role in HC formation in real engines. Despite these limitations, the CFD model successfully replicates the overall UHC emission trend as a function of engine speed.

In general, the minor deviations observed between CFD predictions and experimental data can be attributed to several inherent modeling constraints. These include fixed boundary conditions in CFD that do not fully capture real-world fluctuations in intake temperature, fuel-air mixing, humidity, and injector performance. Moreover, although mesh independence and model sensitivity studies (including turbulence, flame speed, and reaction kinetics) were rigorously conducted, the

approximations inherent to numerical simulation still limit perfect replication of physical experiments. It is also worth noting that real engine systems experience aging, wear, and sensor variability, which introduce uncertainty into experimental measurements. In contrast, simulations rely on idealized geometries and steady-state conditions. Additionally, complex flow structures such as intake-generated swirl and tumble, cyclic variability, and transient spray-wall interactions may not be completely resolved in RANS-based models. Nonetheless, the agreement observed in the brake performance, combustion pressure, and key emission profiles—within approximately  $\pm 10\%$  of the experimental results—supports the robustness and reliability of the developed 3D ICC CFD model for the Renault F8Q engine under full-load conditions.

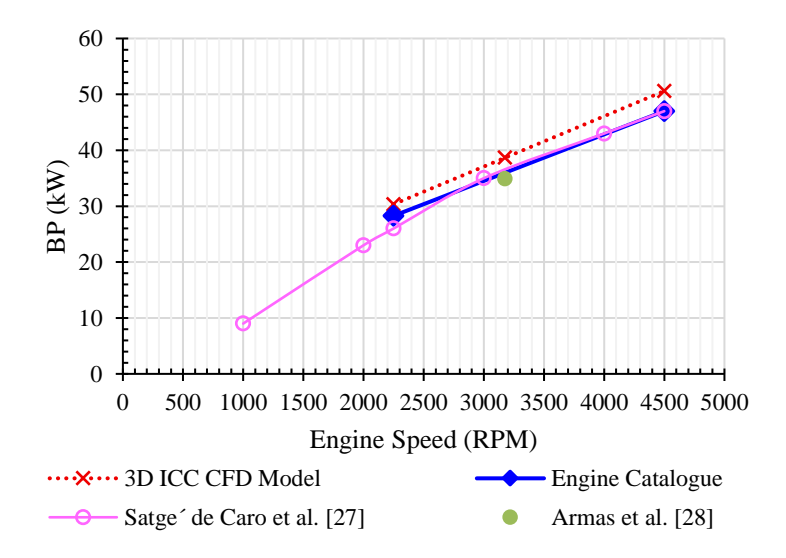


Figure 10. Validation of CFD-based brake performance against experimental literature data

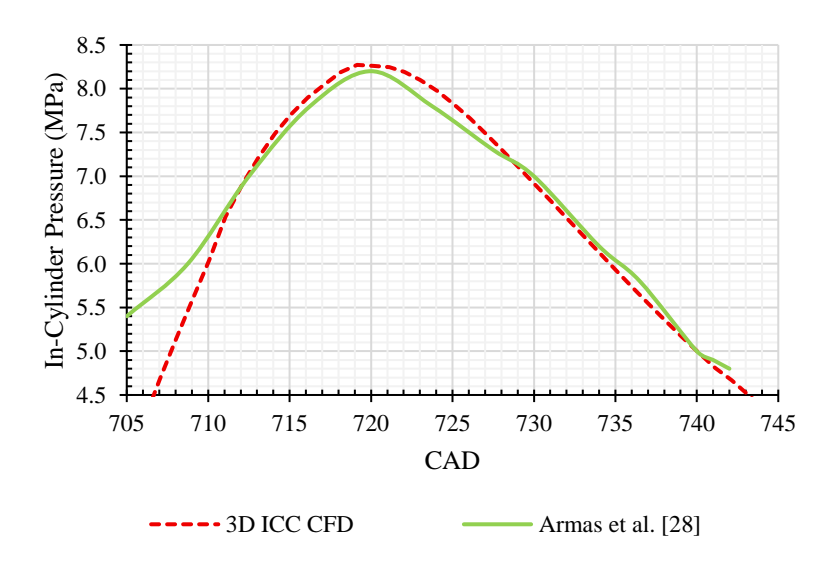


Figure 11. Validation of CFD-based in-cylinder pressure against experimental literature data

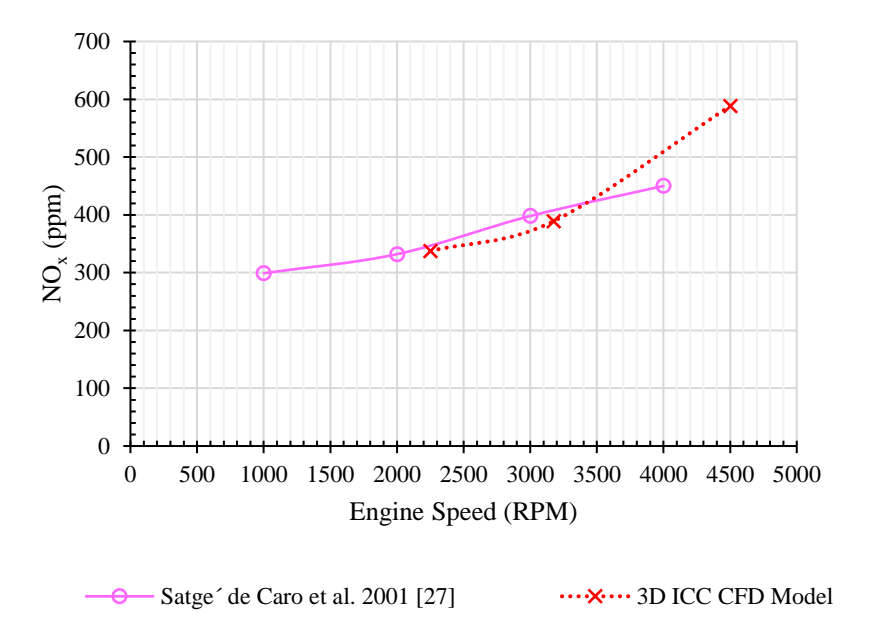


Figure 12. Validation of CFD-based NO<sub>x</sub> against experimental literature data

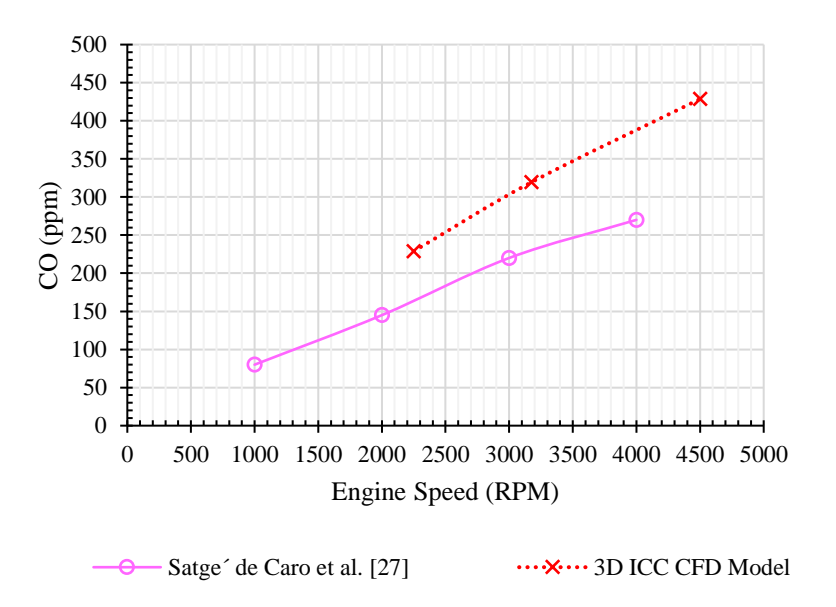


Figure 13. Validation of CFD-based CO against experimental literature data

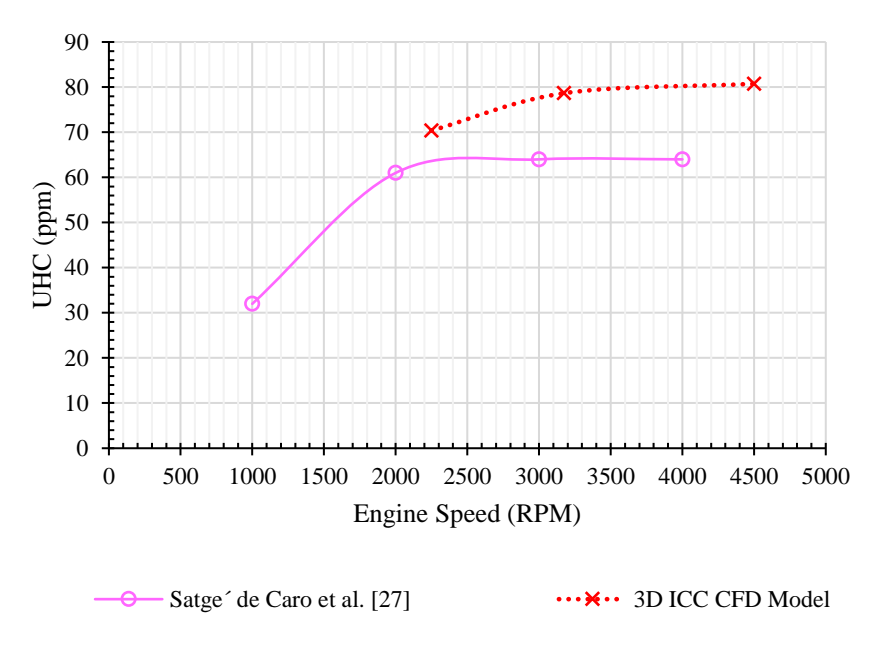


Figure 14. Validation of CFD-based UHC against experimental literature data

## 3.6. 3D ICC CFD Model Simulation Results

In this study, comparative simulations for DMC fuel were conducted using the 3D ICC CFD model, which had been developed through extensive sensitivity analyses and validated against literature-based experimental tests. The selected this fuel was chosen for their potential applicability in CI engines. Including fossil diesel as the reference fuel, a total of two simulations were performed under full load and 2250 RPM operating conditions.

The in-cylinder pressure profiles derived from the CFD simulations are presented as indicator diagrams in Figure 15, allowing a comparative assessment of combustion phasing and peak pressure behavior across all fuel types. In addition, core engine performance parameters were evaluated as a function of fuel composition. Following the fundamental methodology of the 3D ICC CFD model, these parameters were calculated as indicated values and compared accordingly. Indicated torque, indicated power and IMEP are compared in Figure 16, while ISFC is presented in Figure 17, and thermal efficiency comparisons are shown in Figure 18. Figure 19 further provides the in-cylinder radial temperature contours captured adjacent to the injector. Collectively, these visualizations offer a comprehensive assessment of how DMC influences flame development, combustion efficiency, and overall engine performance under identical operating conditions.

The pressure–volume (PV) diagram in Figure 15 clearly demonstrates significant variations in combustion characteristics among the tested fuels at full load and 2250 rpm. In terms of in-cylinder peak pressures, DMC fuel experience peak pressure is higher than diesel. As shown in Table 6, DMC, with its high cetane number and Increased combustion efficiency due to oxygenate additive, low enthalpy of vaporization, leading to the highest peak in-cylinder pressure. The embedded oxygen within DMC's molecular structure facilitates local oxidation reactions even under fuel-rich zones, thereby supporting more complete combustion.

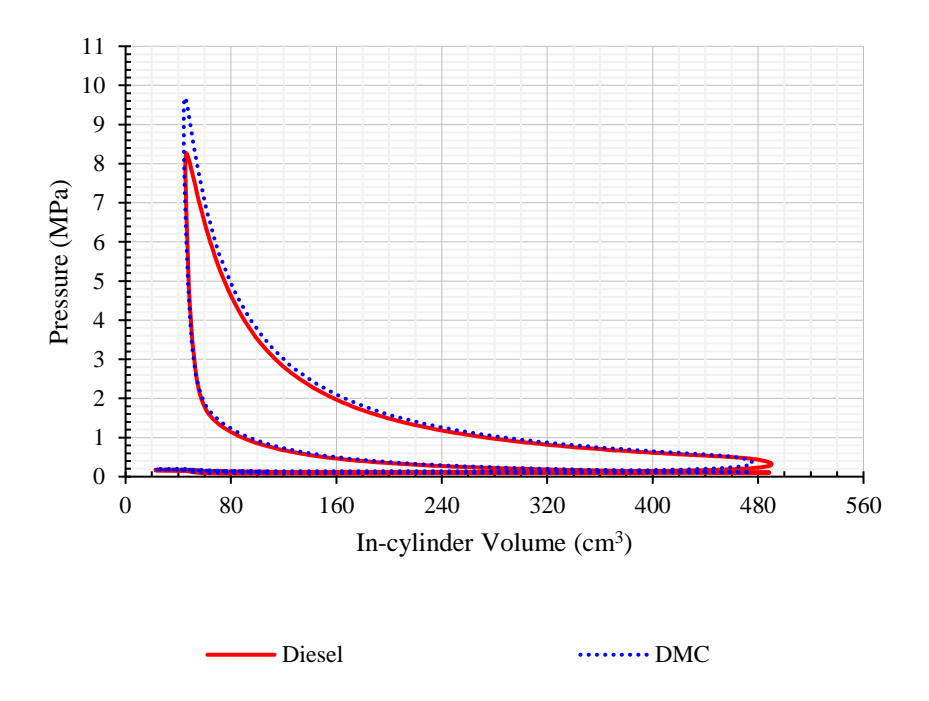
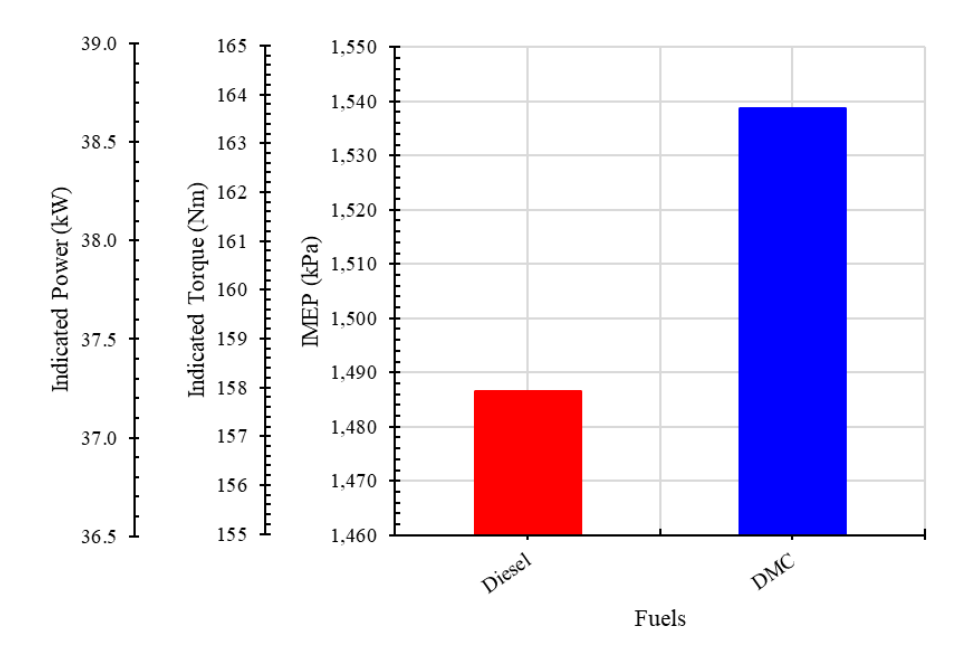


Figure 15. PV diagram for all fuels in 3D ICC CFD simulations

As also shown in Table 6, literature reports emphasize that DMC, owing to its low cetane number and superior atomization capability during injection, mixes more effectively with air upon entering the combustion chamber [21, 47]. This enhanced mixing improves the premixed ratio and combustion rate, which delays the start of combustion while simultaneously increasing in-cylinder pressure and heat release rate. Moreover, the addition of oxygenated fuels has been associated with prolonged ignition delay and elevated heat release during premixed combustion processes [48, 49]. As further indicated in Table 6, the latent heat of vaporization of DMC is higher than that of diesel. Studies in the literature involving various fuels suggest that, due to this property, DMC may absorb more heat during vaporization, which could enhance intake air charging by cooling the charge mixture [50]. Consequently, engine performance may be indirectly improved. In this study, the

same mechanism was observed to increase the indicated torque and indicated power by approximately 3.5% compared to diesel. Since torque, power, and IMEP are interrelated parameters, all three exhibited a proportional increase, providing a performance advantage over diesel and aligning well with previously reported findings.



**Figure 16.** Torque/power/IMEP for all fuels

As shown in Figure 17, DMC exhibited a 4.24% increase in indicated specific fuel consumption (ISFC) compared to diesel. This outcome is primarily influenced by its lower heating value (LHV) and combustion rate. The BSFC parameter of fuels is closely related to their LHV values [50-52]. As indicated in Table 6, the LHV of DMC is 68.87% lower than that of diesel. Despite this, DMC still demonstrated only a limited increase in BSFC, which highlights its favorable combustion behavior. This observation is consistent with the findings reported in the literature [21].

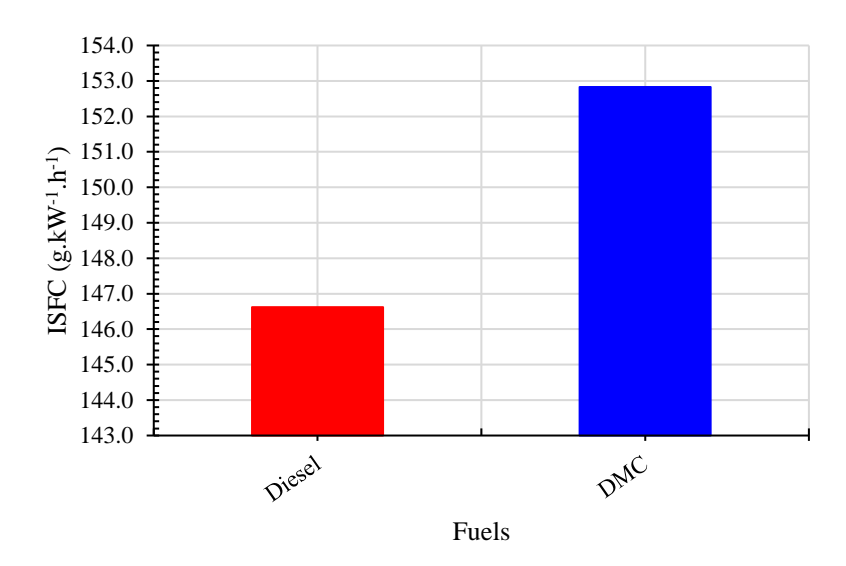


Figure 17. ISFC for all fuels

In the thermal efficiency comparison shown in Figure 18, it is seen that the thermal efficiency of DMC is decreased by 4.06% compared to diesel. These variations directly reflect differences in lower heating value, oxygen content, and combustion phasing across the tested fuels. Since thermal efficiency is fundamentally a consequence of combustion behavior, the trends observed in pressure and performance metrics are consistently mirrored here.

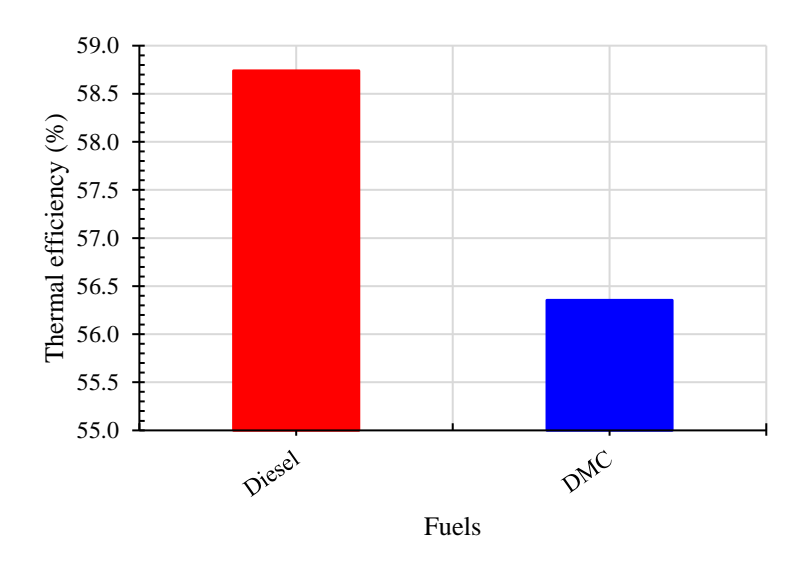


Figure 18. Thermal efficiency for all fuels

The in-cylinder temperature contours shown in Figure 19 further corroborate these performance trends. As combustion progresses from the early to late crank angles, DMC demonstrates a more

widespread and uniform high-temperature distribution compared to diesel. This behavior aligns with its lower cetane number, which delays autoignition and promotes extended fuel—air mixing prior to combustion. The enhanced atomization and oxygen content of DMC contribute to more efficient premixed combustion, resulting in elevated peak cylinder temperatures and improved heat release characteristics. Additionally, the higher latent heat of vaporization of DMC, as noted in Table 6, facilitates greater charge cooling during the intake phase, potentially increasing air density and improving volumetric efficiency. These combined effects lead to a more complete and intense combustion process, thereby enhancing indicated torque and power output. The observed temperature fields are consistent with the 3.5% improvement in performance metrics relative to diesel, supporting the conclusion that DMC offers thermodynamic advantages in compression ignition engines under the tested conditions.

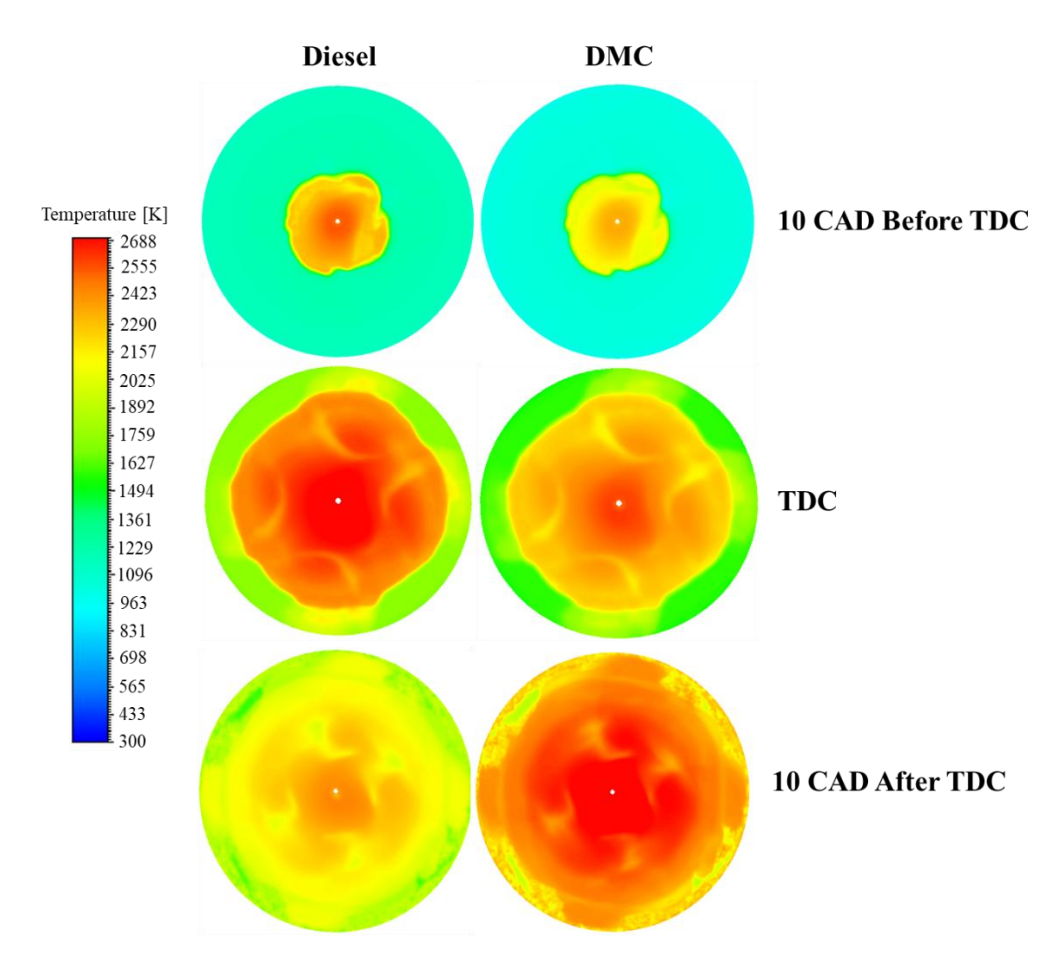


Figure 19. In-cylinder temperature radial contours for all fuels in 3D ICC CFD model

Table 10 presents the simulated emissions of carbon monoxide (CO), unburned hydrocarbons (UHC), and nitrogen oxides (NO<sub>x</sub>) for Diesel and DMC fuels using the validated 3D ICC CFD

model. These emissions were evaluated on a per-cycle basis, providing insight into how fuel type influences combustion stability, efficiency, and pollutant formation in compression ignition (CI) engines. The results indicate that DMC outperformed conventional Diesel by reducing CO and UHC emissions by approximately 13% and 3%, respectively. These findings are consistent with previous studies highlighting the emissions-reducing potential of oxygenated synthetic fuels [53]. Owing to its superior atomization characteristics compared to Diesel, DMC undergoes more complete combustion, leading to reduced CO and UHC emissions [54]. Regarding NO<sub>x</sub> emissions, DMC exhibited a slightly higher level (342.521 ppm) than Diesel, which is likely attributed to more advanced combustion phasing and elevated local in-cylinder temperatures. It is well established that NO<sub>x</sub> formation is directly influenced by in-cylinder combustion temperatures [55]. Additionally, the combination of prolonged ignition delay and high temperatures at advanced crank angles contributes to this increase in NO<sub>x</sub> emissions [21]. In summary, while DMC demonstrates clear advantages in reducing CO and UHC, it is accompanied by a marginal rise in NO<sub>x</sub> reflecting a typical trade-off observed with high-oxygen content fuels.

**Table 10.** Emissions for 3D ICC CFD model

<b>Emissions/Fuels</b>	Diesel	DMC
CO, ppm	228.874	198.544
UHC, ppm	70.384	68.114
NO <sub>x</sub> , ppm	337.383	342.521

#### 4. CONCLUSIONS AND RECOMMENDATIONS

In this study, a comprehensive numerical investigation was conducted to evaluate the combustion, performance, and emission characteristics of DMC fuels in a Renault F8Q compression ignition engine using a fully validated 3D ICC CFD model. The model development was based on experimental literature data, and extensive sensitivity analyses were performed to ensure mesh, time-step, turbulence, and heat transfer model independency. Following model validation, fuel comparison simulations were carried out at 2250 rpm and full load conditions.

The simulation results revealed that DMC offers notable advantages over conventional Diesel in terms of combustion quality and pollutant reduction. Due to its superior atomization capability and high oxygen content, DMC enhanced fuel—air premixing and combustion uniformity, leading to approximately 3.5% higher indicated torque and power. Despite its lower heating value, the

combustion efficiency of DMC was favorable, resulting in only a moderate increase in ISFC and

a relatively small decline in thermal efficiency. In-cylinder temperature contours supported these

findings by showing more homogeneous and elevated peak temperatures during DMC combustion.

From an emissions standpoint, DMC reduced CO and UHC emissions by 13% and 3%,

respectively, highlighting its cleaner combustion profile. However, it caused a slight increase in

NO<sub>x</sub> emissions, primarily due to delayed ignition and elevated in-cylinder temperatures—

characteristics typically observed with oxygenated fuels.

Based on these findings, DMC emerges as a viable alternative fuel for diesel engines, particularly

where reductions in CO and UHC emissions are prioritized. Nevertheless, its slightly higher NO<sub>x</sub>

emissions call for further exploration of advanced injection strategies, EGR application, or

aftertreatment systems to mitigate this drawback. Future studies are recommended to investigate

part-load operation, cold-start behavior, cyclic variability, and aging effects in real engine systems.

Additionally, experimental validation of DMC behavior under transient conditions and with

varying injection timing could provide a more comprehensive understanding of its real-world

applicability.

## **NOMENCLATURE**

n: Engine speed

ρ: Density

k: Number of species

**Φ**: Average of convection term

 $\Gamma$ : Average of the nonlinear convection term

H: Ensemble mean of the convection term

r: Distance

DI: Direct Injection

CFD: Computational Fluid Dynamics

3D ICC: 3D in-Cylinder Combustion

TDC: Top Dead Center

**BDC: Bottom Dead Center** 

rpm: Revolutions per minute

ppm: Parts per million

BP: Brake Power

BMEP: Brake Mean Effective Pressure

BSFC: Brake Specific Fuel Consumption

IP: Indicated Power

IMEP: Indicated Mean Effective Pressure

ISFC: Indicated Specific Fuel Consumption

#### DECLARATION OF ETHICAL STANDARDS

The author of the paper submitted declares that nothing which is necessary for achieving the paper requires ethical committee and legal-special permissions.

### **CONTRIBUTION OF THE AUTHORS**

Emrah Kantaroğlu: Conceptualization, Analysis; Writing- review & editing.

#### CONFLICT OF INTEREST

There is no conflict of interest in this study.

#### REFERENCES

- [1] Martins J, Brito F P. Alternative fuels for internal combustion engines. Energies 2020; 13(16): 4086.
- [2] Kantaroğlu E. CFD-based analysis of performance and emissions in an i-DSI engine using various E-fuels and Syngas. Flow Turbul. Combust. 2025. https://doi.org/10.1007/s10494-025-00660-9
- [3] Serrano J R, Novella R, Piqueras P. Why the development of internal combustion engines is still necessary to fight against global climate change from the perspective of transportation. Appl. Sci. 2019; 9(21): 4597.
- [4] Liu H, Yu S, Wang T, Li J, Wang Y. A systematic review on sustainability assessment of internal combustion engines. J. Clean. Prod. 2024; 451: 141996.
- [5] Liu C, Li Q. Air pollution, global warming and difficulties to replace fossil fuel with renewable energy. Atmos. Climate Sci. 2023; 13(4): 526–538.
- [6] Filonchyk M, Peterson M P, Zhang L, Hurynovich V, He Y. Greenhouse gases emissions and global climate change: Examining the influence of CO<sub>2</sub>, CH<sub>4</sub>, and N<sub>2</sub>O. Sci. Total Environ. 2024; 935: 173359.
- [7] United Nations. Framework Convention on Climate Change. Paris Agreement 2015.

https://unfccc.int/sites/default/files/resource/parisagreement\_publication.pdf. Access: 10.08.2025.

- [8] Leach F, Kalghatgi G, Stone R, Miles P. The scope for improving the efficiency and environmental impact of internal combustion engines. Transp. Eng. 2020: 1; 100005.
- [9] Kantaroğlu E, Doğan A. Experimental investigation of the effects of JP8 and amorphous elemental boron additives on combustion characteristics for i-DSI engine. Int. J. Engine Res. 2025; 26(6): 885-902.
- [10] Gray N, McDonagh S, O'Shea R, Smyth B, Murphy J D. Decarbonising ships, planes and trucks: An analysis of suitable low-carbon fuels for the maritime, aviation and haulage sectors. Adv. Appl. Energy 2021; 1: 100008.
- [11] Schmuch R, Wagner R, Hörpel G, Placke T, Winter M. Performance and cost of materials for lithium-based rechargeable automotive batteries. Nat. Energy 2018; 3: 267–278.
- [12] Roy H, Roy B N, Hasanuzzaman M, Islam M S, Abdel-Khalik A S, Hamad M S, Ahmed S. Global advancements and current challenges of electric vehicle batteries and their prospects: a comprehensive review. Sustainability 2022; 14(24): 16684.
- [13] Virt M, Zöldy M. An AI-based fuel designer tool for sustainable E-fuel development: Methodology, Validation, and Optimization. Energy and AI 2025; 21: 100583.
- [14] Miles, P. C. Potential of advanced combustion for fuel economy reduction in the light-duty fleet. Proc. SAE High-Efficiency Symp, 1508907. 2018.
- [15] Viscardi R, Bassano C, Nigliaccio G, Deiana P. The potential of E-fuels as future fuels. Energia Ambiente Innovazione 2021; 1: 112–116.
- [16] Boretti A. Advancements in e-fuel combustion systems for a sustainable energy future. Int. J. Hydrogen Energy 2024; 79: 258–266.
- [17] Brynolf S, Taljegard M, Grahn M, Hansson J. Electrofuels for the transport sector: A review of production costs. Renew. Sustain. Energy Rev. 2018; 81(2): 1887–1905.
- [18] Valera-Medina A, Xiao H, Owen-Jones M, David W I F, Bowden P J. Ammonia for power. Progress in Energy and Combustion Science 2018; 69: 63–102.
- [19] Goldmann A, Sauter W, Oettinger M, Kluge T, Schröder U, Seume J R, Friedrichs J, Dinkelacker F. A study on electrofuels in aviation. Energies 2018; 11(2): 392.
- [20] Chan J H, Tsolakis A, Herreros J M, Kallis K X, Hergueta C, Sittichompoo S, Bogarra M. Combustion, gaseous emissions and PM characteristics of Di-Methyl Carbonate (DMC)-gasoline blend on gasoline Direct Injection (GDI) engine. Fuel 2020; 263: 116742.
- [21] Pan M, Qian W, Zheng Z, Huang R, Zhou X, Huang H, Li M. The potential of dimethyl carbonate (DMC) as an alternative fuel for compression ignition engines with different EGR rates.

Fuel 2019; 257: 115920.

- [22] Yang J, Jiang Y, Karavalakis G, Johnson K C, Kumar S, Cocker III D R, Durbin T D. Impacts of dimethyl carbonate blends on gaseous and particulate emissions from a heavy-duty diesel engine. Fuel 2016; 184: 681-688.
- [23] Kumar B R, Saravanan S. Partially premixed low temperature combustion using dimethyl carbonate (DMC) in a DI diesel engine for favorable smoke/NOx emissions. Fuel 2016; 180: 396-406.
- [24] Glaude P A, Pitz W J, Thomson M J. Chemical kinetic modeling of dimethyl carbonate in an opposed-flow diffusion flame. Proceedings of the Combustion Institute 2005; 30(1): 1111-1118.
- [25] Alzueta M U, Salinas P, Millera A, Bilbao R, Abián M. A study of dimethyl carbonate conversion and its impact to minimize soot and NO emissions, Proceedings of the Combustion Institute 2017; 36(3): 3985-3993.
- [26] O'Connell N, Stümpfl D, Höß R, Lechner R. Potential of DMC and PODE as Fuel Additives for Industrial Diesel Engines. Fuels 2025; 6(2): 44.
- [27] de Caro P S, Mouloungui Z, Vaitilingom G, Berge, J. C. Interest of combining an additive with diesel–ethanol blends for use in diesel engines. Fuel 2001; 80(4): 565–574.
- [28] Armas O, Ballesteros R, Martos F J, Agudelo J R. Characterization of light duty diesel engine pollutant emissions using water-emulsified fuel. Fuel 2005; 84(7-8): 1011-1018.
- [29] Engine catalog. Renault F8Q specifications 2025. https://mymotorlist.com/engines/renault/f8q/. Access: 10.08.2025.
- [30] Renault Club engine database 2025. <a href="https://en.renault-club.cz/engine\_detail.php?id=49">https://en.renault-club.cz/engine\_detail.php?id=49</a>. Access: 10.08.2025.
- [31] Mitsubishi Motors Corporation 1996. 11A-0-1 Catalogue. <a href="https://w4a33.com/csm/Manuals/4G9%20Series%20Engine%20Workshop%20Manual%20PWE">https://w4a33.com/csm/Manuals/4G9%20Series%20Engine%20Workshop%20Manual%20PWE</a> E9101-ABCDE.pdf. Access: 10.08.2025.
- [32] Kılıç M. Numerical investigation of nanofluid applications in military system. J. Def. Sci. 2018; 17(1): 101–130.
- [33] Hafiz Nik Ab Rashid N M, Hairuddin A A, Md Rezali K A, Masuri S U, Mossa M A A Numerical study of piston bowl geometries on PFI-HCCI engine performance. J. Mech. Eng. Sci. 2023; 17(4): 9689–9699.
- [34] Kantaroğlu E. Influence of different Reynolds numbers and new geometries on water jacket cooling performance in a CI engine. Proc. Inst. Mech. Eng. Part E: J. Process Mech. Eng. 2024. https://doi.org/10.1177/09544089241260876

[35] Yakhot V, Orszag S A. Renormalization group analysis of turbulence. I. Basic theory. Journal of Scientific Computing 1986; 1(1); 3–51.

- [36] Mahle GmbH. Pistons and engine testing. 1st ed. Vieweg + Teubner, Wiesbaden, 2012.
- [37] Lapuerta M, Armas O, Ballesteros R, Carmona M. Fuel Formulation Effects on Passenger Car Diesel Engine Particulate Emissions and Composition. SAE Technical Paper 2000-01-1850. 2000. https://doi.org/10.4271/2000-01-1850
- [38] Han Z, Reitz R D. Turbulence modeling of internal combustion engines using RNG κ-ε models. Combust. Sci. Technol. 1995; 106(4–6): 267–295.
- [39] Plengsa-ard C, Kaewbumrung M. CFD modelling wall heat transfer inside a combustion chamber using ANSYS Forte. IOP Conf. Ser. Mater. Sci. Eng. 2018; 297: 012036.
- [40] First M. Investigation of multistage injection strategies in a DISI engine fueled with methane under stratified charge lean combustion conditions. Environ. Prog. Sustain. Energy 2020; 39(5): 13402.
- [41] Verma I, Bish E, Kuntz M, Meeks E, Puduppakkam K, Naik C, Liang L. CFD modeling of spark ignited gasoline engines—Part 1: Modeling the engine under motored and premixed-charge combustion mode. SAE Tech. Pap. 2016; 2016-01-0591.
- [42] Aktaş F. Numerical investigation of the effects of engine speed on performance and combustion characteristics on a converted spark-ignition natural gas engine. Gazi Univ. J. Sci. Part C Des. Technol. 2022; 10(3): 613–626.
- [43] Rahman K M. Experimental investigation and CFD simulation of mixture formation and combustion in hydrogen direct injection spark-ignition engine. PhD Thesis, Okayama University, 2018.
- [44] Aktaş F, Aytaç Z, Yücel N. Numerical investigation of in-cylinder swirl motion under cold start conditions in a diesel engine. International Journal of Energy Studies 2025; 10(1): 1185–1202.
- [45] O'Rourke P J, Amsden A A. A particle numerical model for wall film dynamics in port-injected engines. SAE Tech. Pap. 1996; 961961.
- [46] Sorrentino, M, Mauramati F, Arsie I, Cricchio A, Pianese C, Nesci W. Application of Willans Line method for internal combustion engines scalability towards the design and optimization of eco-innovation solutions. SAE Tech. Pap. 2015; 2015-24-2397.
- [47] Xiaolu L, Hongyan C, Zhiyong Z, Zhen H. Study of combustion and emission characteristics of a diesel engine operated with dimethyl carbonate. Energy Conversion and Management 2006; 47(11–12): 1438-1448.

[48] Wang H W, Huang Z H, Zhou L B, Jiang D M, Yang Z L. Investigation on emission characteristics of a compression ignition engine with oxygenated fuels and exhaust gas recirculation. Proc Inst Mech Eng, Part D: J Automobile Eng. 2000; 214(5): 503–508.

- [49] Huang Z H, Wang H W, Chen H Y, Zhou L B, Jiang D M. Study of combustion characteristics of a compression ignition engine fuelled with dimethyl ether. Proc Inst Mech Eng, Part D: J Automobile Eng. 1999; 213(6): 647–652.
- [50] Kantaroğlu E, Yontar A A, Doğu Y. Influence of acetone addition into gasoline for i-DSI engine. Sādhanā 2022; 47(1): 14.
- [51] Canakci M. Performance and emissions characteristics of biodiesel from soybean oil. Proc Inst Mech Eng, Part D: J Automobile Eng. 2005; 219(7): 915–922.
- [52] Asokan M A, Prabu S S, Kumar Bade P K, Nekkanti V M, Gopal Gutta S S. Performance, combustion and emission characteristics of juliflora biodiesel fuelled DI diesel engine. Energy 2019; 173: 883–892.
- [53] Abdel-Rahman A A. On the emissions from internal combustion engines: A review. Int. J. Energy Res. 1998; 22(6): 483–513.
- [54] Ramesh T, Sathiyagnanam A P, De Poures M V, Murugan P. A Comprehensive study on the effect of dimethyl carbonate oxygenate and EGR on emission reduction, combustion analysis, and performance enhancement of a CRDI diesel engine using a blend of diesel and prosopis juliflora biodiesel. International Journal of Chemical Engineering 2022; 2022(1): 5717362.
- [55] Kethudaoglu G, Aktaş F, Karaaslan S, Polat S, Dinler N. Investigation of conversion of a diesel engine to homogeneous charge compression ignition engine using n-heptane: A zero-dimensional modeling. International Journal of Energy Studies 2023; 8(3): 535-556.